

High-performance 4-nm-resolution X-ray tomography using burst ptychography

<https://doi.org/10.1038/s41586-024-07615-6>

Received: 28 June 2023

Accepted: 28 May 2024

Published online: 31 July 2024

 Check for updates

Tomas Aidukas¹✉, Nicholas W. Phillips^{1,6}, Ana Diaz¹, Emilia Poghosyan¹, Elisabeth Müller¹, A. F. J. Levi², Gabriel Aepli^{1,3,4,5}, Manuel Guizar-Sicairos^{1,4} & Mirko Holler¹✉

Advances in science, medicine and engineering rely on breakthroughs in imaging, particularly for obtaining multiscale, three-dimensional information from functional systems such as integrated circuits or mammalian brains. Achieving this goal often requires combining electron- and photon-based approaches. Whereas electron microscopy provides nanometre resolution through serial, destructive imaging of surface layers¹, ptychographic X-ray computed tomography² offers non-destructive imaging and has recently achieved resolutions down to seven nanometres for a small volume³. Here we implement burst ptychography, which overcomes experimental instabilities and enables much higher performance, with 4-nanometre resolution at a 170-times faster acquisition rate, namely, 14,000 resolution elements per second. Another key innovation is tomographic back-propagation reconstruction⁴, allowing us to image samples up to ten times larger than the conventional depth of field. By combining the two innovations, we successfully imaged a state-of-the-art (seven-nanometre node) commercial integrated circuit, featuring nanostructures made of low- and high-density materials such as silicon and metals, which offer good radiation stability and contrast at the selected X-ray wavelength. These capabilities enabled a detailed study of the chip's design and manufacturing, down to the level of individual transistors. We anticipate that the combination of nanometre resolution and higher X-ray flux at next-generation X-ray sources will have a revolutionary impact in fields ranging from electronics to electrochemistry and neuroscience.

Many engineered and natural systems are hierarchies of subsystems characterized by length scales varying over ten orders of magnitude between the atomic and the macroscopic. Important examples are integrated circuits, which are typically several millimetres wide and with the smallest features approaching the atomic scale. At the time of writing, there are 7-nm node (a measure of transistor density) integrated circuits in consumer products and the 3-nm node is starting production. For quality control and reverse engineering, the necessary multiscale inspection starts with optical microscopies and conventional X-ray tomography, followed by nanometre-level inspection using electron microscopy. Scanning electron microscopy (SEM) probes only the sample surface and can be sensitive to surface charging, and transmission electron microscopy is effective for only thin (5–100 nm) slices⁵. For three-dimensional (3D) imaging, overcoming the poor penetration of electrons (owing to the strong interaction of charged particles with matter) necessitates a 'slice and view' approach, where single-layer imaging alternates with destructive ion-milling, suffering from cutting artefacts, charging and anisotropic resolution¹.

In contrast to the 1–30-keV or 100–300-keV electrons generally used for SEM and transmission electron microscopy, respectively⁶, hard X-rays (>5 keV) can penetrate 10–500-μm-thick samples⁷ and, given their short wavelength, should allow subnanometre resolution. Achieving high

resolution with transmission X-ray microscopy (TXM) requires hardware stability on the order of nanometres and high-numerical-aperture lenses. Despite the lens manufacturing challenges, the 3D resolution of TXM was improved recently from 50 nm (ref. 8) to 10 nm (ref. 9) for absorption-based imaging. However, many sample types show little-to-no absorption contrast owing to their weak interaction with X-rays, necessitating the use of phase-imaging techniques, such as Zernike phase contrast¹⁰. Unfortunately, phase imaging using TXM requires additional hardware, which increases the experimental complexity, reduces the resolution and lowers the light collection efficiency. More importantly, the resolution of 3D imaging scales with the radiation dose, following an inverse power law of 1/dose^{1/4} (ref. 11), and, given the limited efficiency of X-ray lenses, sub-10-nm TXM imaging is probably limited to specimens that have exceptional radiation resistance.

To circumvent the limitations of TXM and provide quantitative phase contrast, lensless-imaging techniques such as ptychography have emerged^{12–14}. During ptychographic data collection, the sample is scanned across a coherent X-ray beam, and a far-field diffraction pattern is collected for each scanning position. Once the desired field of view is scanned, iterative algorithms applied to the recorded diffraction patterns recover the amplitude and phase of the sample transmissivity. Ptychography provides diversity to the measurement

¹Paul Scherrer Institute, Villigen, Switzerland. ²Department of Electrical and Computer Engineering, University of Southern California, Los Angeles, CA, USA. ³Department of Physics, Eidgenössische Technische Hochschule Zürich (ETH Zürich), Zurich, Switzerland. ⁴Institute of Physics, École Polytechnique Fédérale de Lausanne (EPFL), Lausanne, Switzerland. ⁵Quantum Center, Eidgenössische Technische Hochschule Zürich (ETH Zürich), Zurich, Switzerland. ⁶Present address: Mineral Resources, CSIRO, Clayton, Victoria, Australia. [✉]e-mail: tomas.aidukas@psi.ch; mirko.holler@psi.ch

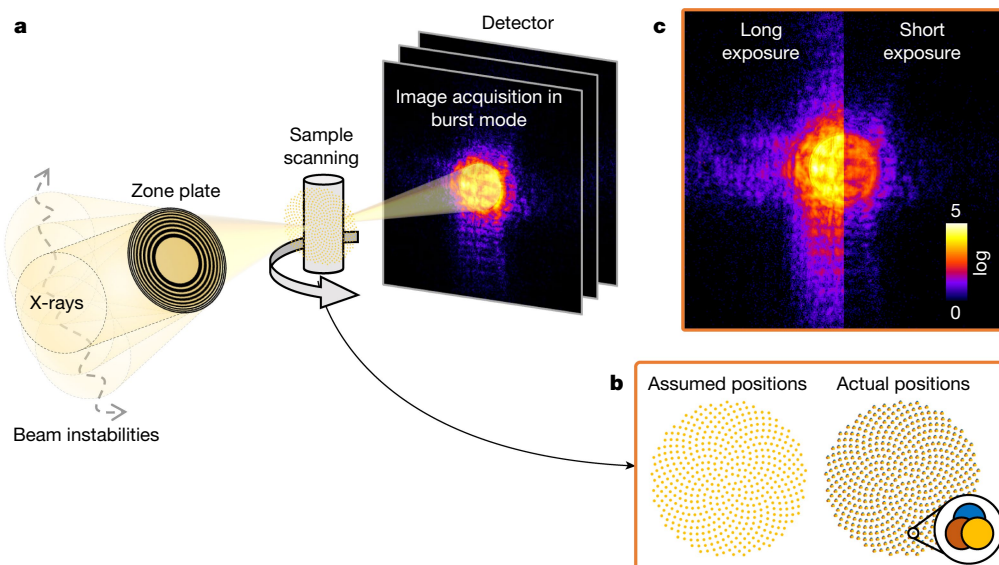


Fig. 1 | Illustration of experimental instabilities and burst data acquisition.

a, In burst ptychographic X-ray tomography, many diffraction patterns are recorded for each sample scanning position and rotation angle. **b**, In the presence of wavefront instabilities, the actual beam positions near the focus will deviate from the idealized assumption. To account for instabilities computationally, we record a time-resolved series of diffraction patterns using multiple

short-exposure images in burst mode for each scanning position. An example is shown in Supplementary Video 1. **c**, Compared with the long-exposure acquisition, burst images feature higher speckle visibility as they minimize motion blur, but suffer individually from low photon count. The colour bar shows the number of photons captured by the detector on a logarithmic scale.

through overlapped illumination¹⁵, which, together with computational optimization routines^{16,17}, solves the missing-phase problem provided that the forward model, that is, the mathematical description of light interaction with matter and its propagation to the detector, is accurate. Ptychography can be combined with sample rotation to generate ptychographic X-ray computed tomography (PXCT)^{2,3,18}, which bridges the 3D resolution gap between conventional X-ray imaging and electron microscopy.

In 2017, Holler et al. imaged an integrated circuit using then state-of-the-art PXCT with an isotropic 3D resolution of 15.4 nm (ref. 18), and, more recently, Michelson et al. surveyed a 2-μm-diameter nanoparticle superlattice sample with 7-nm 3D resolution³. Our work builds on these achievements by leveraging enhanced instrumentation^{19,20} and data collection and reconstruction algorithms, to image a 5-μm-diameter integrated circuit with a 4.2-nm 3D resolution. Reaching such resolving power using 6.2-keV X-rays results in a depth of field 10-times smaller than the 5-μm sample diameter, which was mitigated by a back-propagation tomography reconstruction method^{4,21}, representing, to our knowledge, the first known application of this approach in X-ray microscopy. Owing to innovations presented in this paper, we achieved a five-times-smaller-resolution voxel volume, compared with Michelson et al.³, and a two orders of magnitude faster data acquisition rate of 14,000 3D resolution elements per second (calculated by dividing the number of collected resolution elements by the time it took to collect the data, including the measurement overheads). Furthermore, we demonstrate segmentation of the 3D volume according to material, allowing detailed association of electronic functionality, for example, transistor and electrical interconnect, with morphology.

Burst ptychography

Exceptional imaging performance necessitates high-precision sample scanning^{19,22,23}, state-of-the-art alignment and reconstruction algorithms^{16,17,24} along with dose-efficient data acquisition to compensate for sample deformations²⁵. Despite precise positioning, environmental, instrumental and illumination instabilities can still blur diffraction patterns and degrade data quality.

As X-ray imaging resolution approaches the nanometre scale, measures similar to those in electron microscopy are necessary. The introduction of four-dimensional scanning transmission electron microscopes²⁶ with high-speed, pixelated detectors marked a significant advance in electron microscopy by enabling faster imaging and instability mitigation through post-processing^{27,28}. Likewise, high-speed scanning in X-ray ptychography has achieved sub-20-nm resolution^{29–31}, which in combination with low-exposure detection has enhanced robustness against instabilities³². An alternative and complementary approach that can mitigate experimental inconsistencies with respect to the assumed forward model is the mixed-state ptychography reconstruction method³³ and orthogonal probe relaxation³⁴. Although mixed-state ptychography is frequently utilized to account for partial coherence of illumination, it has been also demonstrated to mitigate experimental instabilities³⁵ or motion artefacts, particularly in continuous sample-scanning experiments^{23,29}. However, sample and/or probe motion during data acquisition reduces contrast of the far-field diffraction patterns and compromises the reconstruction quality³⁶.

To overcome the experimental instabilities that currently limit PXCT, we implement burst ptychography, a technique illustrated in Fig. 1, where for each scan position we collect multiple low-exposure frames before moving to the next scan point. To maintain the necessary radiation dose at each scan position, the required exposure time is divided among multiple frames. This comes at the cost of larger data volume and high shot noise of the individual low-exposure burst frames, which we mitigate by a specialized reconstruction pipeline that identifies and groups similar frames. A high-speed data acquisition and processing workflow was recently introduced to measure temporal fluctuations of magnetic states imaged holographically, using an iterative hierarchical clustering algorithm³⁷. Our approach, akin to that employed successfully for two-dimensional single-particle imaging using an X-ray free-electron laser³⁸, embeds temporal fluctuation identification directly into a ptychographic reconstruction framework, allowing scanning instability identification and correction with subpixel accuracy¹⁷, as described in Methods. As part of the ptychographic optimization framework, position refinement adjusts the assumed positions to

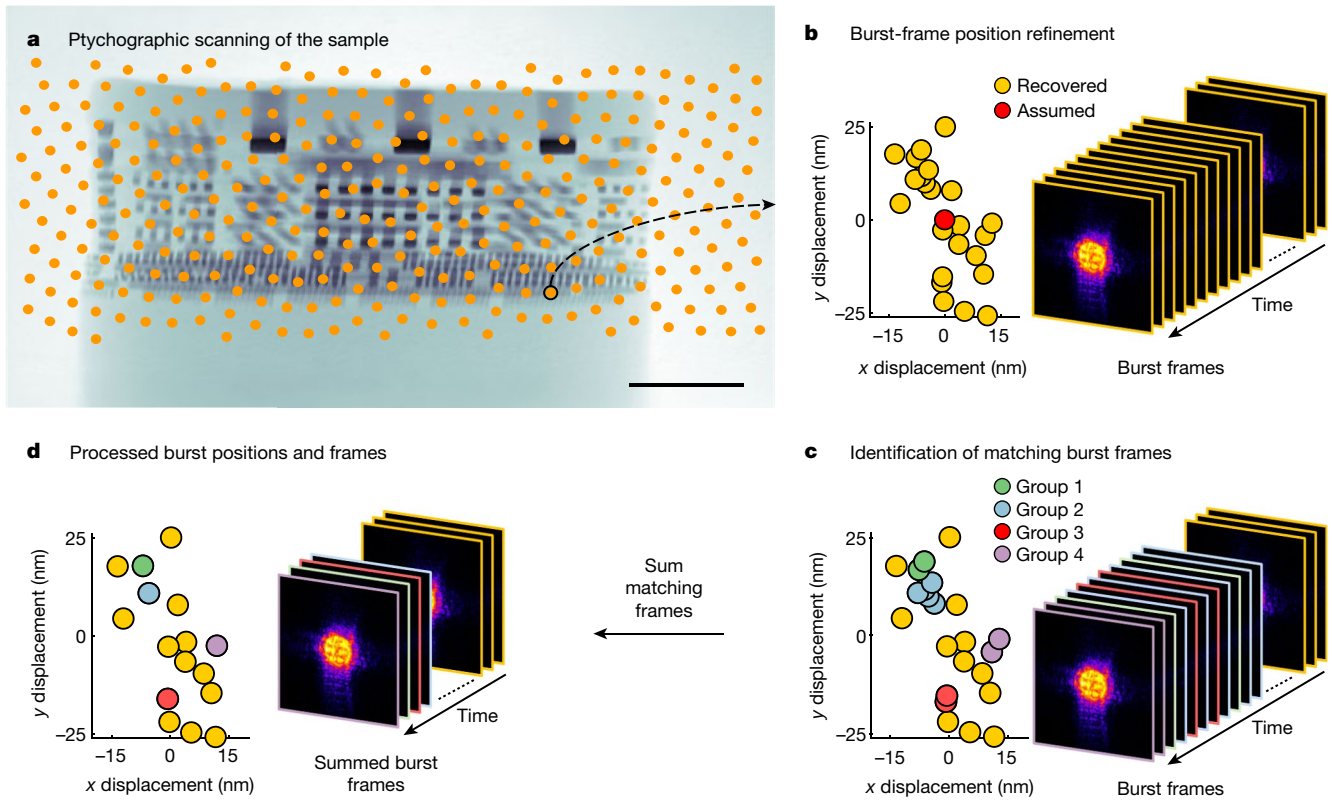


Fig. 2 | Burst ptychography data reconstruction workflow. **a**, Ptychographic phase projection of the sample, with scanning positions shown as yellow points. Scale bar, 1 μm . **b**, Recovered illumination positions across all burst frames within a single scan point. The positions were recovered by ptychographic position refinement and show ± 25 -nm instabilities at the sample plane.

c,d, By identifying (**c**) and summing (**d**) matching burst frames, the signal-to-noise ratio is increased while simultaneously reducing the reconstructed data size and computational demands. Such reconstruction workflows enable high-resolution ptychography even with an unstable X-ray beam, provided that the detection is fast enough to temporally resolve the instabilities.

maintain consistency between the experimental data and the image formation model based on the well-established diffraction theory of light. To assess the superior performance of burst ptychography, we compare it with mixed-state ptychography in Methods.

depth of field. The complete description of our burst ptychography reconstruction workflow can be found in Methods.

Workflow

The integrated circuit chosen for inspection was an AMD Ryzen 5 5600G Processor, fabricated using current commercial Taiwan Semiconductor Manufacturing Company (TSMC) 7-nm Fin Field Effect Transistor (FinFET) technology. The imaging tool was an upgraded PXCT instrument¹⁹ at the coherent small-angle X-ray scattering beamline, located at the Swiss Light Source. Burst ptychography data acquisition and reconstruction were necessary to recover and correct for X-ray beam instabilities occurring during projection acquisition. The collection of 23 burst frames for each sample scan position enabled the recovery of instabilities, showing a beam movement amplitude of ± 25 nm at the sample plane, as depicted in Fig. 2a,b, primarily attributed to the angular motion of the X-ray beam incident on the illumination-generating Fresnel zone plate. Once the data were acquired, the signal-to-noise ratio of each noisy burst frame was significantly improved during computational post-processing by identifying and summing matching burst frames based on the refined position similarity, as illustrated in Fig. 2c,d. On average, the summation of burst frames decreased the number of diffraction patterns to be processed during ptychographic reconstruction by 30–40%. Once processed, the resulting high-resolution projections were aligned with subpixel accuracy²⁴ and a back-propagation reconstruction algorithm⁴ was used to reconstruct an absorption and a quantitative phase tomogram, providing a tenfold increase in the

Comparison between X-ray imaging and electron microscopy

The outcome of the measurement and analysis workflow is a 3D tomogram of the AMD processor, where each voxel contains quantitative measures of the X-ray absorption and phase contrast. Given the significantly lower absorption contrast, only the X-ray phase projections were used for subsequent visualization. To verify the reconstruction quality, a cross-sectional cut was extracted from the reconstructed PXCT tomogram in Fig. 3a,b and compared with images acquired using SEM and bright-field scanning transmission electron microscopy (BF-STEM) in Fig. 3c,d. For the latter, we used a thin lamella cut from an area of the integrated circuit adjacent to the region from which the PXCT pillar was extracted. Thus, the BF-STEM image in Fig. 3c represents an interaction volume with 50–100-nm thickness, whereas the PXCT reconstruction in Fig. 3b is a 4.2-nm thin slice through the sample volume.

For comparison, we identified distinct components of the FinFET transistor that are present in both samples, such as the U-shaped gates shown in Fig. 3e, top left, and the contacts shown in Fig. 3e, bottom left. The qualitative comparison was also supplemented by normalized line profiles across the U-shaped gates shown in Fig. 3e, top left. Using BF-STEM as a reference, the bright gate outline is around 4–5-nm thick and is of higher density than the interior. Despite being just 1-pixel wide, PXCT is capable of resolving the gate outline as shown by the image and line profile in Fig. 3e, top left. Although the contrast and fidelity of some features imaged by BF-STEM are superior to PXCT, it is important to

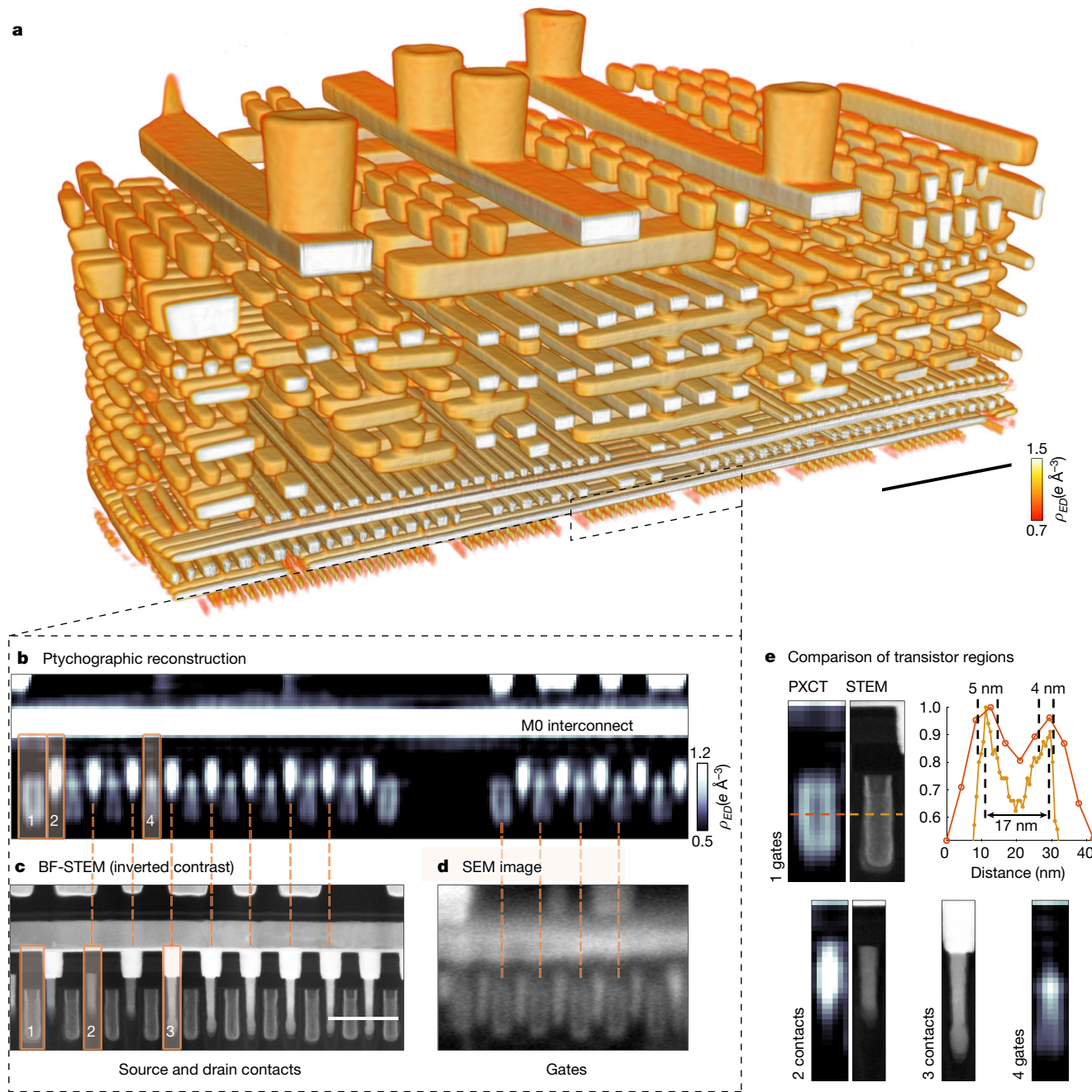


Fig. 3 | Comparison of transistor images obtained by X-ray imaging and electron microscopy. **a**, A 3D rendering of the reconstructed tomogram, with 4.2-nm resolution, reveals half the volume to show the interior of the integrated circuit, with the full rendering shown in Supplementary Video 2. Scale bar, 1 μm . **b–d**, Different circuit sections were analysed using both X-ray imaging and electron microscopy showing consistent gate and contact pitches (marked with orange dashed line, respectively). Moreover, **d** highlights how charging artefacts degrade image quality in SEM compared with PXCT. For a direct comparison of X-ray imaging and electron microscopy, distinct transistor features in similar regions were examined using PXCT (**b**) and contrast-inverted BF-STEM (**c**),

analysed further in **e**. Scale bar in **c**, 100 nm. **e**, Expanded images of regions 1–4 in **b,c**. Although features in the left images (1 (gates) and 2 (contacts)) are similar in both datasets, the bottom middle and right images (3 (contacts) and 4 (gates)) show either physical or contrast-related differences. Furthermore, line cuts (top right) along the dashed lines in the top left images through the U-shaped gates indicate that PXCT can resolve gate outlines as narrow as 4–5 nm. It is noted that the BF-STEM images are two-dimensional projections of 50–100-nm-thick lamella whereas the PXCT images represent computed sections with a 4.2-nm thickness. The colour bars show electron density in units of electrons per cubic angstrom.

note that the BF-STEM resolution was as low as 0.66 nm (limited by the pixel size), which is 6-times smaller than the 4.2-nm pixel size of PXCT.

Despite the spatial proximity of the BF-STEM and PXCT samples, the structural maps of the transistor layers shows significant differences. For example, the contact shown in Fig. 3e, bottom middle, is connected to the upper M0 interconnect layer, unlike the contacts in Fig. 3e, bottom left. Other differences include the unique gate

structure shown in Fig. 3e, bottom right, which is observed only in PXCT images. Unlike the U-shaped gates from Fig. 3e, top left, such gates, whose exact function is unknown to us given that we are not in possession of the design files for the chip, could be the so-called dummy gates used to maintain the thermal and structural stability of the transistor unit cell³⁹. Differences between PXCT and BF-STEM can be attributed not only to the different sample volumes, with very

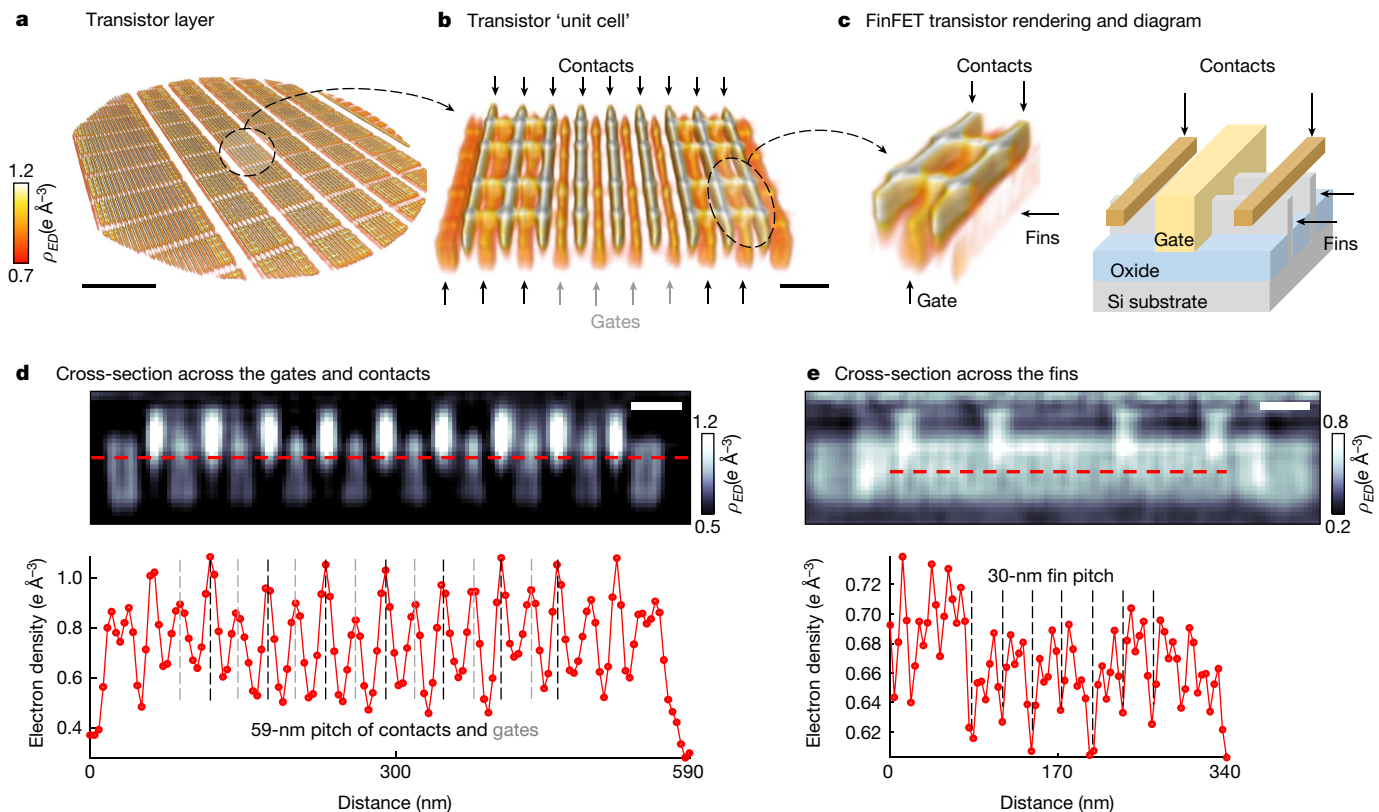


Fig. 4 | Structural analysis of the FinFET transistor layer. **a**, A 3D rendering of the reconstructed tomogram exposing the lower transistor layer of the integrated circuit. **b**, The characteristic transistor unit cell is repeated throughout the entire bottom layer of the sample. **c**, In addition to the gates and contacts, the fins are a crucial component of the FinFET transistor design.

d, The cross-section of the reconstruction shows the gates and contacts with their characteristic 59-nm pitch. **e**, Looking at the cross-section perpendicular to **d**, lower material density structures are seen with a 30-nm pitch, which is expected for the fins. Scale bars, 1 μm (**a**), 100 nm (**b**), 50 nm (**d,e**). The colour bars show electron density in units of electrons per cubic angstrom.

different thicknesses, being imaged but also to the different contrast mechanism. Furthermore, although PXCT provides quantitative electron-density values at every voxel, BF-STEM image contrast will be affected by factors such as dynamical scattering, limited detector dynamic range and the projected structure size within the lamella. For example, the bright structure connecting the contact to the M0 interconnect layer in Fig. 3e, bottom middle, appears brighter, implying a density higher than that of the contact. However, on the basis of the energy-dispersive X-ray spectroscopy shown in Extended Data Fig. 7, the structure is primarily composed of silicon, whereas the contact contains significantly heavier elements such as cobalt. Such discrepancies are probably owing to the different extension of the features along the projection direction within the volume of the lamella (thin contact versus thick silicon structure). Nevertheless, the observed similarities in FinFET transistor components lend credibility to the features observed within the PXCT images.

Structural analysis of the FinFET transistor

The lowest layer of an integrated circuit, as shown in Fig. 4a, contains a variety of circuits designed for a specific task. In our sample, the characteristic unit-cell circuits in Fig. 4b are repeated throughout the bottom layer. In addition to the gates and contacts, Fig. 4c shows crucial FinFET components, which include the fins intersecting the gates from a perpendicular direction and the source and drain contacts touching the fins. On the basis of the cross-sectional analysis in Fig. 4d, each unit cell has a U-shaped gate at both sides of the cell and alternating gates and contacts in-between with a 59-nm pitch, matching the expected design rules for a 7-nm-node FinFET transistor⁴⁰.

Moreover, the zoom-in of the U-shaped gate cross-section in Fig. 3e, top left, shows that the distance between the high-density material encapsulating the gate is approximately 17 nm, which is only 4-pixels wide, matching the expected design parameters⁴⁰. The reconstruction cross-section in Fig. 4e at a perpendicular direction to Fig. 4d shows evidence of low-density structures with a 30-nm pitch, which matches the expected fin pitch⁴⁰. As the fins should be around 7-nm wide⁴⁰, the ability to see them within a tomogram with a 4.2-nm voxel size supports our high-resolution claims. However, to completely resolve and analyse the fin structure, the higher resolving power of future PXCT is necessary. Supplementary Videos 2–4 and Extended Data Fig. 9 provide an overview of the transistor layer.

Resolution estimation

The resolution of the reconstructed tomogram was determined to be limited by the 4.2-nm voxel size, based on the Fourier shell correlation (FSC) analysis shown in Extended Data Fig. 8 and described in Methods. By performing the FSC analysis on well-sampled data that follow the Crowther sampling criterion^{2,41}, the resolution estimate is obtained as an average along all reciprocal-space directions. In addition, the predictable directionality of the copper connectors in the lower integrated circuit layers makes them ideally suited for resolution estimation using edge profile analysis. The width over which the edge height increases from 25% to 75% is known as the 25–75 edge response criterion⁴². This criterion is half of the Rayleigh resolution and it corresponds to the half-pitch resolution, whereas the Rayleigh criterion defines full-pitch resolution. On the basis of Extended Data Fig. 8, the half-pitch resolution is around 4.2 nm, validating the FSC analysis.

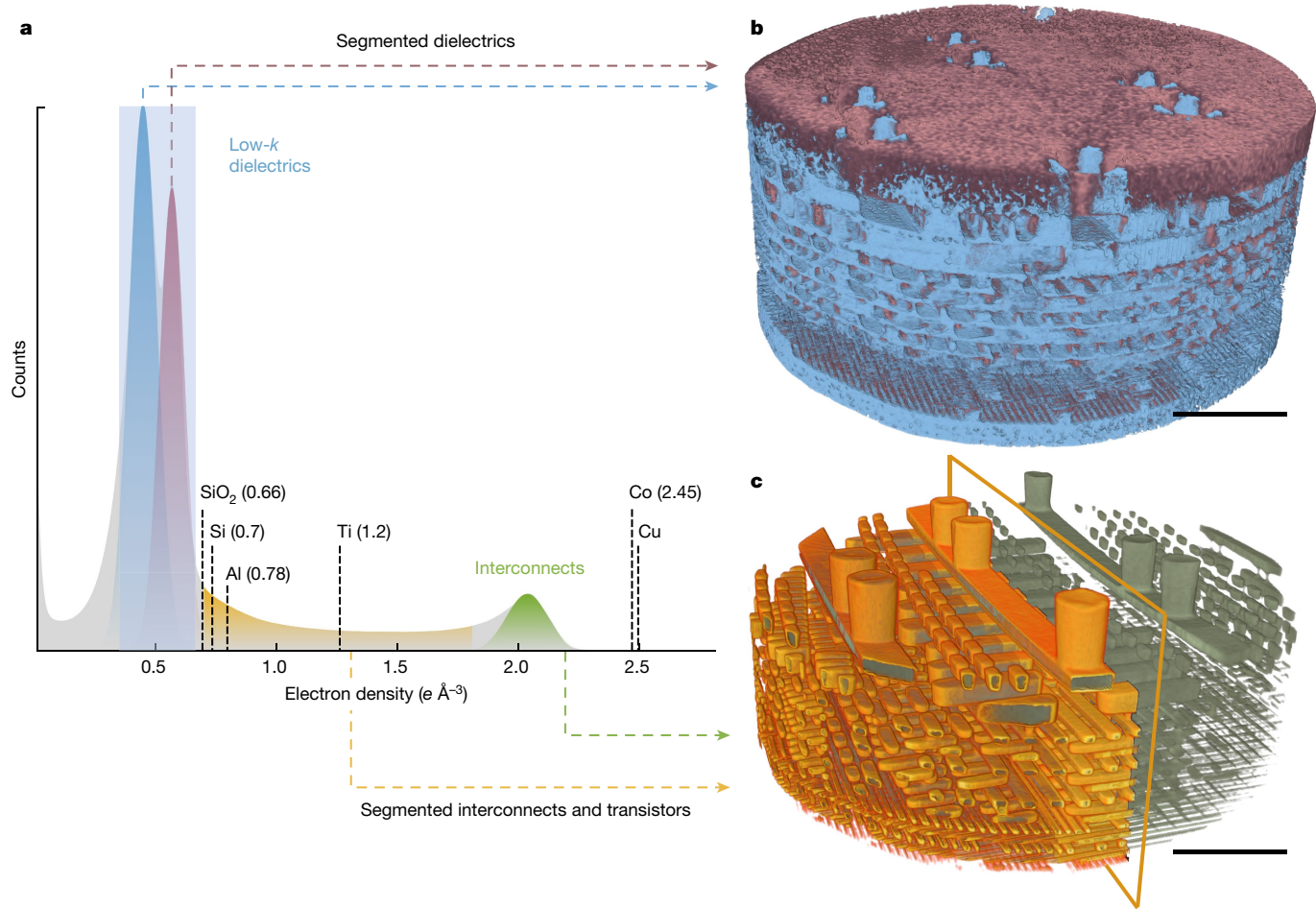


Fig. 5 | Quantitative composition characterization of the integrated circuit. **a**, Histogram of the reconstructed electron-density tomogram segmented into four distinct material phases. **b,c**, The two lowest-density materials represent the dielectrics (**b**), whereas the highest-density region

(green) can be assigned to the interconnects (**c**). The remaining region in yellow represents the transistor layer as well as artefacts due to partial volume effects. Scale bars, 1 μm.

Segmentation according to material

Integrated circuits are complex systems consisting of different networks formed from different materials. In particular, the interconnects are metal conductors, insulated from each other by a dielectric material and ultimately linked to the gates, sources and drains of the transistors in the lower layers of the integrated circuit. As the interconnects and transistors become smaller, the risk of increased parasitic charge build-up and crosstalk between the interconnects increases. To minimize charge leakage and improve the overall performance of the integrated circuits, frequently used dielectrics such as silicon dioxide (SiO_2) have been replaced by so-called low- k materials with a lower dielectric constant k (ref. 43). Lower k values can be achieved by incorporating other elements into the silica network, such as fluorine or organic groups such as CH_3 , to reduce the dielectric polarizability⁴³. As mass density for a given class of materials is strongly related to the dielectric constant k , PXCT can separate dielectrics with differing k values based on the reconstructed electron density⁴⁴. (Electron density can be computed via $\rho = \rho_{\text{ED}} M / (N_A N_e)$, where ρ_{ED} is the electron density, M is the molar mass, N_A is the Avogadro number and N_e is the number of electrons within a molecule)⁴⁴.

The histogram of the reconstructed volume in Fig. 5a reveals three distinct material phases within the integrated circuit having electron densities of $0.44 \text{ e } \text{\AA}^{-3}$, $0.55 \text{ e } \text{\AA}^{-3}$ and $2.05 \text{ e } \text{\AA}^{-3}$, where 1 \AA equals 10^{-10} m . The metal of choice for modern integrated circuit interconnects is copper (Cu), which is patterned by the Damascene process,

where thin Cu films are deposited onto the dielectric substrate⁴⁵. Key properties such as resistivity depend on the deposition method, for example, electroplating or chemical vapour deposition. Although bulk Cu has a mass density of 8.94 g cm^{-3} ($2.45 \text{ e } \text{\AA}^{-3}$ electron density), Cu films can have densities as low as 6.9 g cm^{-3} ($1.9 \text{ e } \text{\AA}^{-3}$ electron density)⁴⁶, explaining the 7.5 g cm^{-3} ($2.05 \text{ e } \text{\AA}^{-3}$ electron density) density recovered by PXCT. The remaining electron densities of $0.44 \text{ e } \text{\AA}^{-3}$ and $0.55 \text{ e } \text{\AA}^{-3}$ can be assigned to low- k dielectric materials, which have a lower density than the $0.65 \text{ e } \text{\AA}^{-3}$ (2.22 g cm^{-3}) of SiO_2 . For example, the density of carbon-doped silica (SiCOH) can be as low as 1.17 – 1.43 g cm^{-3} (refs. 47,48). However, the ratio of Si, C, O and H atoms in SiCOH varies depending on the manufacturing process, requiring additional information to identify the exact chemical composition and mass density. A complementary analysis using energy-dispersive X-ray spectroscopy is provided in Methods, which confirms the presence of two dielectric materials and Cu-containing interconnects.

The reconstructed volume was segmented into subnetworks fabricated from materials with differing densities. The reconstructed volume contains a higher- k dielectric ($0.55 \text{ e } \text{\AA}^{-3}$ electron density) in the upper layers, which is necessary to insulate the large interconnects shown in Fig. 5b. As the interconnect dimensions decrease towards the lower integrated circuit layers, a lower- k dielectric ($0.45 \text{ e } \text{\AA}^{-3}$ electron density) is used to insulate the closely packed conductors. Given the density differences between dielectrics and metals, PXCT can readily distinguish the interconnects and transistors from the surrounding dielectric, as shown in Fig. 5c. Although Cu is the dominating interconnect

material, the transistor layer is composed of elements with a density lower than that of Cu. However, given the complex composition (see the energy-dispersive X-ray spectroscopy data in Extended Data Fig. 7) and presence of subpixel-sized features at the transistor layer, quantitative analysis of the composition becomes unreliable owing to partial volume effects.

Discussion

With X-ray burst ptychography, we have achieved a resolution of 4.2 nm in 3D, essential for high-resolution tasks such as inspecting nanoscale integrated circuits. This resolution was enabled by identifying and mitigating X-ray beam instabilities with subpixel accuracy, pushing the limits of X-ray nanotomography without requiring nanometre beam stability. Our adaptable reconstruction workflow is applicable to current ptychography instruments, provided that the detector can record images faster than the underlying instabilities. Demonstrated on complex systems such as integrated circuits, this technique holds significant promise for broader applications in both artificial and biological systems. Our results reinforce previous claims¹⁸ about the potential of ptychography, particularly with advances in X-ray sources, optics and detectors.

The source of the vibrational errors during our measurement was instability of the monochromator owing to the nitrogen cooling of its first crystal, which operates at 40 Hz. The vibrations cause the outgoing X-rays to change the incidence angle on the beam-shaping X-ray lens, which was positioned 5.4 m away, resulting in an estimated 550–920-nrad angular perturbation of the X-ray illumination. This leads to translational errors of approximately 20–35 nm at the sample plane near the focus, consistent with the recovered positions shown in Fig. 2. Such translational errors are equivalent to scanning positioning errors and can be corrected through position refinement^{15–17} during ptychographic reconstruction.

If the monochromator has imperfections, these structural features will be imprinted onto the X-ray beam. When instabilities are present, the X-ray beam structure will appear to undergo temporal variations during the ptychographic data acquisition, violating the static illumination assumption in ptychography. To minimize these effects, we use highly aberrated Fresnel zone plates for beam-shaping, such that the engineered beam structure is stronger than the wavefront variations²⁰. Moreover, significant wavefront changes can be algorithmically mitigated by reconstructing a unique illumination beam at each scan position using the orthogonal probe relaxation algorithm³⁴, allowing burst ptychography to accommodate both temporal probe variations and random scanning instabilities.

The achievable imaging resolution is significantly influenced by the material composition of the sample, which affects X-ray scattering and radiation damage. The widest X-ray scattering angle, and the maximum attainable resolution, depend on the electron-density contrast between materials within the sample. For instance, integrated circuits, containing low-density silicon-based dielectrics and high-density metals such as copper, provide the strong density contrast required for high-resolution imaging⁴⁹. Solid oxide fuel cells and catalysts are also composites of transition metals and lighter elements, and therefore similarly suited for high-resolution imaging.

As the resolution scales inversely with the fourth power of the required dose¹¹, high-resolution imaging requires radiation-resistant samples. While integrated circuits are considered radiation resistant, our sample deformed significantly, although the lowest layers containing the transistors deformed the least, probably owing to the enhanced dissipation of heat and electrical charging through the denser metallic structures. The sample absorbed a high radiation dose of 6.26×10^{10} Gy, but we have observed radiation-induced changes to this specific integrated circuit even at 1–2 orders of magnitude lower doses. The suspected cause is the presence of radiation-sensitive low-*k*

dielectric materials, containing light elements such as carbon. As the algorithmic correction for these deformations is challenging²⁵, achieving even higher resolution will necessitate dose-sparing image acquisition methods, which, for example, take advantage of prior information such as Graphic Design System (GDS) files in the case of integrated circuits. Also, deformations can be reduced via different sample mounting (for example, for laminography⁵⁰, the sample is a large planar section of a chip rather than a thin and more vulnerable pillar) and imaging at cryogenic temperatures⁵¹.

The 5-μm diameter of our sample exceeded the 0.5-μm depth-of-field limit of our imaging system, set by resolution and X-ray illumination wavelength⁵². Overcoming depth-of-field limitations in ptychography usually involves multi-slice reconstruction, where multiple slices within the sample are reconstructed along the X-ray path^{52,53}. However, this reconstruction is computationally intensive and can suffer from poor convergence depending on the data quality and chosen slice thicknesses. An alternative approach is to apply a filtered back-propagation tomographic reconstruction algorithm, frequently used in optical diffraction tomography⁴, which has until now—to our knowledge—not been employed for X-rays. Assuming our sample to be weakly scattering and employing single-slice ptychography, we significantly extended the depth of field via filtered back-propagation, thus challenging existing depth-of-field enhancement methods in PXCT⁵⁴, and also opening opportunities for further research.

In summary, burst ptychography has enabled us to reconstruct an integrated circuit volume with features as small as 4.2 nm, despite the challenges posed by radiation damage, depth-of-field limitations and experimental beam instabilities. Our proposed tomographic and ptychographic algorithms are poised to facilitate further high-resolution experiments under less-than-ideal imaging conditions at synchrotrons, free-electron lasers and small laboratory-based X-ray sources.

Online content

Any methods, additional references, Nature Portfolio reporting summaries, source data, extended data, supplementary information, acknowledgements, peer review information; details of author contributions and competing interests; and statements of data and code availability are available at <https://doi.org/10.1038/s41586-024-07615-6>.

1. Utke, I., Moshkalev, S. & Russell, P. *Nanofabrication Using Focused Ion and Electron Beams: Principles and Applications* (Oxford Univ. Press, 2012).
2. Dierolf, M. et al. Ptychographic X-ray computed tomography at the nanoscale. *Nature* **467**, 436–439 (2010).
3. Michelson, A. et al. Three-dimensional visualization of nanoparticle lattices and multimaterial frameworks. *Science* **376**, 203–207 (2022).
4. Kak, A. C. & Slaney, M. *Principles of Computerized Tomographic Imaging* Classics in Applied Mathematics Vol. 33, 203–273 (Society for Industrial and Applied Mathematics, 2001).
5. Smith, D. J. Atomic-resolution structure imaging of defects and interfaces in compound semiconductors. *Prog. Cryst. Growth Charact. Mater.* **66**, 100498 (2020).
6. Inkson, B. J. in *Materials Characterization Using Nondestructive Evaluation (NDE) Methods* (eds Hübchen, G., Altpeter, I., Tschuncky R. & Hans-Georg, H.) 17–43 (Elsevier, 2016).
7. Deng, J. et al. Nanoscale X-ray imaging of circuit features without wafer etching. *Phys. Rev. B* **95**, 104111 (2017).
8. Wang, J. et al. Automated markerless full field hard X-ray microscopic tomography at sub-50 nm 3-dimension spatial resolution. *Appl. Phys. Lett.* **100**, 143107 (2012).
9. De Andrade, V. et al. Fast X-ray nanotomography with sub-10 nm resolution as a powerful imaging tool for nanotechnology and energy storage applications. *Adv. Mater.* **33**, 2008653 (2021).
10. Holzner, C. et al. Zernike phase contrast in scanning microscopy with X-rays. *Nat. Phys.* **6**, 883–887 (2010).
11. Howells, M. R. et al. An assessment of the resolution limitation due to radiation-damage in X-ray diffraction microscopy. *J. Electron Spectros. Relat. Phenomena* **170**, 4–12 (2009).
12. Rodenburg, J. M. & Faulkner, H. M. A phase retrieval algorithm for shifting illumination. *Appl. Phys. Lett.* **85**, 4795–4797 (2004).
13. Thibault, P. et al. High-resolution scanning X-ray diffraction microscopy. *Science* **321**, 379–382 (2008).
14. Pfeiffer, F. X-ray ptychography. *Nat. Photon.* **12**, 9–17 (2018).
15. Guizar-Sicairos, M. & Fienup, J. R. Phase retrieval with transverse translation diversity: a nonlinear optimization approach. *Opt. Express* **16**, 7264–7278 (2008).

16. Thibault, P. & Guizar-Sicairos, M. Maximum-likelihood refinement for coherent diffractive imaging. *New J. Phys.* **14**, 063004 (2012).
17. Odstrčil, M., Menzel, A. & Guizar-Sicairos, M. Iterative least-squares solver for generalized maximum-likelihood ptychography. *Opt. Express* **26**, 3108–3123 (2018).
18. Holler, M. et al. High-resolution non-destructive three-dimensional imaging of integrated circuits. *Nature* **543**, 402–406 (2017).
19. Odstrčil, M., Lebugle, M., Lachat, T., Raabe, J. & Holler, M. Fast positioning for X-ray scanning microscopy by a combined motion of sample and beam-defining optics. *J. Synchrotron Radiat.* **26**, 504–509 (2019).
20. Odstrčil, M., Lebugle, M., Guizar-Sicairos, M., David, C. & Holler, M. Towards optimized illumination for high-resolution ptychography. *Opt. Express* **27**, 14981–14997 (2019).
21. Müller, P., Schürmann, M. & Guck, J. The theory of diffraction tomography. Preprint at <https://arxiv.org/abs/1507.00466> (2016).
22. Holler, M. & Raabe, J. Error motion compensating tracking interferometer for the position measurement of objects with rotational degree of freedom. *Opt. Eng.* **54**, 054101 (2015).
23. Deng, J. et al. The Velociprobe: an ultrafast hard X-ray nanoprobe for high-resolution ptychographic imaging. *Rev. Sci. Instrum.* **90**, 083701 (2019).
24. Odstrčil, M., Holler, M., Raabe, J. & Guizar-Sicairos, M. Alignment methods for nanotomography with deep subpixel accuracy. *Opt. Express* **27**, 36637–36652 (2019).
25. Odstrčil, M. et al. Ab initio nonrigid X-ray nanotomography. *Nat. Commun.* **10**, 2600 (2019).
26. Ophus, C. Four-dimensional scanning transmission electron microscopy (4D-STEM): from scanning nanodiffraction to ptychography and beyond. *Microsc. Microanal.* **25**, 563–582 (2019).
27. Li, X. et al. Electron counting and beam-induced motion correction enable near-atomic-resolution single-particle cryo-EM. *Nat. Methods* **10**, 584–590 (2013).
28. Gallagher-Jones, M. et al. Nanoscale mosaicity revealed in peptide microcrystals by scanning electron nanodiffraction. *Commun. Biol.* **2**, 26 (2019).
29. Pelz, P. M. et al. On-the-fly scans for X-ray ptychography. *Appl. Phys. Lett.* **105**, 251101 (2014).
30. Huang, X. et al. Fly-scan ptychography. *Sci. Rep.* **5**, 9074 (2015).
31. Jiang, Y. et al. Achieving high spatial resolution in a large field-of-view using lensless X-ray imaging. *Appl. Phys. Lett.* **119**, 124101 (2021).
32. Deng, J. et al. High-resolution ptychographic imaging enabled by high-speed multi-pass scanning. *Opt. Express* **30**, 26027–26042 (2022).
33. Thibault, P. & Menzel, A. Reconstructing state mixtures from diffraction measurements. *Nature* **494**, 68–71 (2013).
34. Odstrčil, M. et al. Ptychographic coherent diffractive imaging with orthogonal probe relaxation. *Opt. Express* **24**, 8360–8369 (2016).
35. Liu, S. et al. Position-guided ptychography for vibration suppression with the aid of a laser interferometer. *Opt. Lasers Eng.* **160**, 107297 (2023).
36. Odstrčil, M., Holler, M. & Guizar-Sicairos, M. Arbitrary-path fly-scan ptychography. *Opt. Express* **26**, 12585–12593 (2018).
37. Klose, C. et al. Coherent correlation imaging for resolving fluctuating states of matter. *Nature* **614**, 256–261 (2023).
38. Daurer, B. J. et al. Ptychographic wavefront characterization for single-particle imaging at X-ray lasers. *Optica* **8**, 551–562 (2021).
39. Du, Y. & Wong, M. D. F. Optimization of standard cell based detailed placement for 16 nm FinFET process. In *2014 Design, Automation & Test in Europe Conference & Exhibition (DATE) 1–6* (IEEE, 2014).
40. Clark, L. T. et al. ASAP7: a 7-nm finFET predictive process design kit. *Microelectron. J.* **53**, 105–115 (2016).
41. Crowther, R. A., DeRosier, D. J. & Klug, A. The reconstruction of a three-dimensional structure from projections and its application to electron microscopy. *Proc. R. Soc. Lond. A* **317**, 319–340 (1970).
42. Attwood, D. (ed.) *Soft X-Rays and Extreme Ultraviolet Radiation: Principles and Applications* 337–394 (Cambridge Univ. Press, 1999).
43. Shamiryan, D., Abell, T., Iacopi, F. & Maex, K. Low-k dielectric materials. *Mater. Today* **7**, 34–39 (2004).
44. Diaz, A. et al. Quantitative X-ray phase nanotomography. *Phys. Rev. B* **85**, 020104 (2012).
45. Cheng, Y.-L. et al. in *Noble and Precious Metals: Properties, Nanoscale Effects and Applications* (eds Singh Seehra, M. & Bristow, A. D.) Ch. 10 (IntechOpen, 2018).
46. Parmigiani, F., Kay, E., Huang, T. C. & Swalen, J. D. Interpretation of the nonbulklike optical density of thin copper films grown under ion bombardment. *Appl. Opt.* **24**, 3335–3338 (1985).
47. Maex, K. et al. Low dielectric constant materials for microelectronics. *J. Appl. Phys.* **93**, 8793–8841 (2003).
48. Lee, H.-J. et al. Characterization of chemical-vapor-deposited low-k thin films using X-ray porosimetry. *Appl. Phys. Lett.* **82**, 1084–1086 (2003).
49. Du, M. et al. Upscaling X-ray nanoimaging to macroscopic specimens. *J. Appl. Crystallogr.* **54**, 386–401 (2021).
50. Holler, M. et al. Three-dimensional imaging of integrated circuits with macro- to nanoscale zoom. *Nat. Electron.* **2**, 464–470 (2019).
51. Holler, M. et al. OMNY PIN—a versatile sample holder for tomographic measurements at room and cryogenic temperatures. *Rev. Sci. Instrum.* **88**, 113701 (2017).
52. Tsai, E. H. R., Usov, I., Diaz, A., Menzel, A. & Guizar-Sicairos, M. X-ray ptychography with extended depth of field. *Opt. Express* **24**, 29089–29108 (2016).
53. Li, P. & Maiden, A. Multi-slice ptychographic tomography. *Sci. Rep.* **8**, 2049 (2018).
54. Tsai, E. H. R. et al. Correlated X-ray 3D ptychography and diffraction microscopy visualize links between morphology and crystal structure of lithium-rich cathode materials. *iScience* **11**, 356–365 (2019).

Publisher's note Springer Nature remains neutral with regard to jurisdictional claims in published maps and institutional affiliations.

Springer Nature or its licensor (e.g. a society or other partner) holds exclusive rights to this article under a publishing agreement with the author(s) or other rightsholder(s); author self-archiving of the accepted manuscript version of this article is solely governed by the terms of such publishing agreement and applicable law.

© The Author(s), under exclusive licence to Springer Nature Limited 2024, corrected publication 2024

Methods

Sample preparation

We purchased an off-the-shelf AMD Ryzen 5 5600G Processor from a mainstream electronics distributor. The integrated circuit cover was removed on a hot plate and cut out from the printed circuit board using a fast-spinning diamond blade. Once glued onto the sample holder, a lapping machine was used to slowly remove the printed circuit board until the bump-bonding region was exposed. The 5- μm -diameter cylindrical sample was extracted from a randomly selected location using a focused ion beam (FIB)/SEM providing a focused gallium beam for milling and an electron beam for imaging with the in-lens detector (Zeiss, NVision40). The milled sample was extracted using a micro-manipulator and mounted onto an OMNY pin⁵¹ (Extended Data Fig. 1) using the carbon deposition in the FIB followed by carbon coating. For SEM imaging, we cut into the surface of the integrated circuit with the gallium beam, to give access to the circuit structures for the electron beam. For STEM imaging and energy-dispersive X-ray spectroscopy (EDX), we prepared with the FIB/SEM 50–100 nm thin lamellae of an integrated circuit sample extracted from an adjacent region to the one imaged by PXCT. High-resolution BF-STEM and high-angle annular dark-field (HAADF)-STEM micrographs (Extended Data Figs. 1c, 6 and 7) were acquired using probe-corrected STEM (JeolJEM-ARM200F transmission electron microscope/STEM) operated at 200 keV at the Electron Microscopy Facility, PSI.

Experimental set-up and image acquisition

PXCT measurements were conducted at the coherent small-angle X-ray scattering beamline of the Swiss Light Source using an X-ray beam 0.7- μm in diameter, at the sample plane, at 6.2-keV photon energy. Extended Data Fig. 2 illustrates the experimental set-up, and photographs of the experimental set-up can be found in refs. 22,55. The beam was formed by an iridium Fresnel zone plate (FZP; XRnanotech, Switzerland), with an outermost zone width of 30 nm, zone height of 400 nm, a diameter of 250 μm and a gold, 50- μm -diameter, integrated central stop. The zones of the FZP were purposefully distorted during manufacturing to introduce aberrations into the illumination probe. Such wavefront modulation leads to higher ptychographic reconstruction quality, especially of the lower spatial frequencies^{20,56}. The local zone displacement was designed via computational simulations such that the reconstructed image contrast and resolution are maximized. Hybrid scanning of the FZP and sample was used to speed up measurements and increase the stability of the set-up using active motion feedback¹⁹. The stability and precision of sample scanning were further improved by interferometric correction of the sample stage tilt errors, higher-accuracy FZP scanner sensors¹⁹ and improved interferometric readout electronics. The plots in Extended Data Fig. 2b depict the average instabilities of the scanning stage at each scan position during the acquisition of a single projection, as measured by the interferometer readout at 3.5 kHz. Hence, during the acquisition of ptychographic projections, the average scanning instabilities were approximately 2 nm vertically and 4 nm horizontally, which are below the reconstructed volume resolution of 4.2 nm.

An in-vacuum EIGER 1.5M detector (PSI, Switzerland)⁵⁷, with a pixel size of 75 μm , was used for X-ray detection. An evacuated flight tube was installed between the sample and the detector, with a sample-to-detector distance of 0.788 m. Each two-dimensional ptychography projection covered a sample area of 7.5 \times 3.2 μm^2 with a step size of 0.25 μm following a Fermat spiral pattern⁵⁸. To capture the instabilities of the illuminating beam, a burst of diffraction patterns was captured at each scan position, with a total exposure time of 0.2 s. The total exposure budget at a given scan position was split over 23 burst frames, each having an exposure time of 7.5 ms with a 1-ms dead time (8.5 ms in total). The exposure time of each burst frame was selected to ensure sufficient sampling of the underlying instabilities,

which were assumed to be caused by the nitrogen cryostat cooling the monochromator operating at 40 Hz (25-ms period). Acquisition of a single projection took approximately 80 s and deposited a dose of around 4×10^7 Gy. To achieve a 3D resolution target of 4.2 nm, 1,700 projections were acquired to satisfy tomographic sampling requirements⁴¹ over a period of 38 h and a radiation dose of 6.8×10^{10} Gy was absorbed by the sample.

Ptychographic reconstruction algorithm

To introduce the ptychographic reconstruction method, we assume that an object $O_{\mathbf{r}_i}$ is scanned across an X-ray probe $P_{\mathbf{r}}$. This interaction at each scan position i generates an exit wave $\psi_{\mathbf{r}_i}^m$ (ref. 16):

$$\psi_{\mathbf{r}_i} = O_{\mathbf{r}_i} P_{\mathbf{r}}, \quad (1)$$

where \mathbf{r} is the real-space location of the sample relative to the X-ray probe and i is a scalar position index value. Such multiplicative formulation assumes that the object is optically thin, simplifying the interaction to a single scattering event. The exit wave then propagates to a detector, forming a far-field diffraction pattern whose intensity, $I_{\mathbf{k}_i}$, is expressed by:

$$I_{\mathbf{k}_i} = |\Psi_{\mathbf{k}_i}|^2 = |\mathcal{F}\{O_{\mathbf{r}_i} P_{\mathbf{r}}\}|^2, \quad (2)$$

where $\Psi_{\mathbf{k}_i} = \mathcal{F}\{\psi_{\mathbf{r}_i}\}$ denotes the Fourier-transformed exit wave, linking real-space interactions to reciprocal-space (\mathbf{k}) observations.

To find the object $O_{\mathbf{r}}$ and the probe $P_{\mathbf{r}}$, ptychographic reconstruction can be cast as an optimization problem, minimizing the squared difference between the measured and estimated amplitudes:

$$\operatorname{argmin}_{O_{\mathbf{r}}, P_{\mathbf{r}}} \sum_{\mathbf{r}} |I_{\mathbf{k}_i} - |\mathcal{F}\{O_{\mathbf{r}_i} P_{\mathbf{r}}\}||^2, \quad (3)$$

Although multiple formulations of equation (3) exist, maximum-likelihood estimation methods have shown that minimizing the difference between the amplitudes rather than intensities gives superior performance in the presence of Poisson noise^{16,59,60}.

To solve equation (3), ptychographic reconstruction can be formulated as a joint optimization problem in real and reciprocal domains, described by the following cost functions:

$$\mathcal{L}_{r,i} = \sum_{\mathbf{r}} |O_{\mathbf{r}_i} P_{\mathbf{r}} - \psi_{\mathbf{r}_i}^e|^2, \quad (4)$$

$$\mathcal{L}_{k,i} = \sum_{\mathbf{r}} |I_{\mathbf{k}_i} - |\Psi_{\mathbf{k}_i}^e||^2. \quad (5)$$

The goal is to iteratively refine the estimations of the exit wave in reciprocal space by utilizing the measured diffraction images and then apply the corrections in real space to improve estimations of both the object and the probe. In the ptychographic reconstruction process, the estimated exit wave $\Psi_{\mathbf{k}_i}^e$ in reciprocal space is refined by employing a gradient descent approach to minimize the cost function outlined in equation (5). The update is formulated as^{16,17,59,60}:

$$\Psi_{\mathbf{k}_i}^{e'} = \Psi_{\mathbf{k}_i}^e - \frac{\partial \mathcal{L}_{k,i}}{\partial (\Psi_{\mathbf{k}_i}^e)^*} = \Psi_{\mathbf{k}_i}^e \frac{\sqrt{|I_{\mathbf{k}_i}|}}{|\Psi_{\mathbf{k}_i}^e|}, \quad (6)$$

where $\partial \mathcal{L}_{k,i} / \partial (\Psi_{\mathbf{k}_i}^e)^*$ is the Wirtinger derivative of the cost function with respect to the complex conjugate of $\Psi_{\mathbf{k}_i}^e$ (refs. 16,17,60). This derivative provides the direction for updating $\Psi_{\mathbf{k}_i}^e$, aiming to reduce the discrepancy between the measured and predicted diffraction patterns. The solution in equation (6) is the well-known detector support constraint used for conventional phase retrieval⁶¹, where the reconstructed amplitude is replaced by the measured amplitude.

Article

After updating the reciprocal-space estimate, the exit wave is transformed back to real space via $\psi_{\mathbf{r}_i}^e = \mathcal{F}^{-1}\{\psi_{\mathbf{k}_i}^e\}$ and used for the minimization of the cost function in equation (4) to obtain the object and the probe updates using first-order gradient descent:

$$P'_{\mathbf{r}} = P_{\mathbf{r}} - \beta_i \frac{\partial \mathcal{L}_{r,i}}{\partial P_{\mathbf{r}}^*}, \quad (7)$$

$$O'_{\mathbf{r}_i} = O_{\mathbf{r}_i} - \alpha_i \frac{\partial \mathcal{L}_{r,i}}{\partial O_{\mathbf{r}_i}^*}, \quad (8)$$

where α_i and β_i are the step sizes for the probe and object updates, respectively. The gradients of the cost function with respect to the complex conjugates of the probe and object functions yield the search direction for the iterative updates:

$$\Delta P_{\mathbf{r}_i} = \frac{\partial \mathcal{L}_{r,i}}{\partial P_{\mathbf{r}}^*} = \sum_{\mathbf{r}} 2O_{\mathbf{r}_i}^*(O_{\mathbf{r}_i}P_{\mathbf{r}} - \psi_{\mathbf{r}_i}^e), \quad (9)$$

$$\Delta O_{\mathbf{r}_i} = \frac{\partial \mathcal{L}_{r,i}}{\partial O_{\mathbf{r}_i}^*} = \sum_{\mathbf{r}} 2P_{\mathbf{r}}^*(O_{\mathbf{r}_i}P_{\mathbf{r}} - \psi_{\mathbf{r}_i}^e). \quad (10)$$

To improve robustness and convergence, the search directions were calculated for multiple scan positions \mathcal{N} simultaneously and averaged together:

$$\Delta \hat{P}_{\mathbf{r}_i} = \frac{\sum_{i \in \mathcal{N}} \Delta P_{\mathbf{r}_i}}{\sum_{i \in \mathcal{N}} |O_{\mathbf{r}_i}|^2 + \delta_p}, \quad (11)$$

$$\Delta \hat{O}_{\mathbf{r}_i} = \frac{\sum_{i \in \mathcal{N}} \Delta O_{\mathbf{r}_i}}{\sum_{i \in \mathcal{N}} |P_{\mathbf{r}}|^2 + \delta_o}, \quad (12)$$

where δ_o and δ_p are regularization terms that prevent division by values that are close to zero. Once the search directions are known, the probe and object estimates in equations (7) and (8) are updated iteratively by approaching the solution along the weighted mean of the steepest gradient directions:

$$P'_{\mathbf{r}} = P_{\mathbf{r}} - \frac{\sum_{i \in \mathcal{N}} \beta_i \Delta \hat{P}_{\mathbf{r}_i} |O_{\mathbf{r}_i}|^2}{\sum_{i \in \mathcal{N}} |O_{\mathbf{r}_i}|^2}, \quad (13)$$

$$O'_{\mathbf{r}} = O_{\mathbf{r}} - \frac{\sum_{i \in \mathcal{N}} \alpha_i \Delta \hat{O}_{\mathbf{r}_i} |P_{\mathbf{r}}|^2}{\sum_{i \in \mathcal{N}} |P_{\mathbf{r}}|^2}. \quad (14)$$

Moreover, the step sizes α_i and β_i were obtained by an analytical solution of equation (5) using the least-squares method as described in section 2.2 in ref. 17:

$$\beta_i = \frac{\sum_{\mathbf{r}} \mathcal{R}[(O_{\mathbf{r}_i}P_{\mathbf{r}} - \psi_{\mathbf{r}_i}^e)(\Delta O_{\mathbf{r}_i}P_{\mathbf{r}})^*]}{\sum_{\mathbf{r}} |\Delta O_{\mathbf{r}_i}P_{\mathbf{r}}|^2 + \gamma}, \quad (15)$$

$$\alpha_i = \frac{\sum_{\mathbf{r}} \mathcal{R}[(O_{\mathbf{r}_i}P_{\mathbf{r}} - \psi_{\mathbf{r}_i}^e)(\Delta O_{\mathbf{r}_i}P_{\mathbf{r}})^*]}{\sum_{\mathbf{r}} |\Delta O_{\mathbf{r}_i}P_{\mathbf{r}}|^2 + \gamma}, \quad (16)$$

where γ is a small value to avoid divisions close to zero and \mathcal{R} takes the real value of the terms.

The reconstruction algorithm presented in this section is called the least-squares maximum-likelihood (LSQML) reconstruction engine, which was described in detail in ref. 17 and is currently implemented in the open-source reconstruction package called PtychoShelves⁶².

Position refinement algorithm

To recover the X-ray beam instabilities, we used a position refinement algorithm embedded directly into the iterative ptychographic reconstruction. At each iteration, ptychography provides an estimate of the object region illuminated by the X-ray beam at a given scan position. To improve the estimate, it is propagated to reciprocal space, where the reconstructed modulus is replaced by the experimentally measured diffraction pattern amplitude. If the assumed scan position is not correct, there will be a mismatch between the estimated and measured diffraction pattern modulus in reciprocal space. Hence, once the estimate is propagated back to real space, the reconstruction will translate by a small amount to increase consistency with the measured data (such shifts are typically assumed to be subpixel accurate^{17,63}). Therefore, in the presence of positional errors, the estimated exit wave $\psi_{\mathbf{r}_i}^e$ will translate towards the correct solution by a small amount ($\alpha_{x,i}, \alpha_{y,i}$) at each iteration as a result of the ptychographic constraints^{17,63}. The shifted exit wave $\psi_{\mathbf{r}_i + (\alpha_{x,i}, \alpha_{y,i})}^e$ can be assumed to be caused by the relative translation of the probe $P_{\mathbf{r} + (\alpha_{x,i}, \alpha_{y,i})}$ with respect to the object $O_{\mathbf{r}_i}$, leading to the modified cost function from equation (4):

$$\mathcal{L}_{r,i} = \sum_{\mathbf{r}} |O_{\mathbf{r}_i}P_{\mathbf{r} + (\alpha_{x,i}, \alpha_{y,i})} - \psi_{\mathbf{r}_i}^e|^2. \quad (17)$$

Assuming that the shifts are small at any given iteration, a Taylor expansion can be used to approximate the reconstructed probe:

$$P_{\mathbf{r} + (\alpha_{x,i}, \alpha_{y,i})} \approx P_{\mathbf{r}} + \alpha_{x,i} \frac{\partial P_{\mathbf{r}}}{\partial x} + \alpha_{y,i} \frac{\partial P_{\mathbf{r}}}{\partial y}, \quad (18)$$

which leads to the modified cost function in equation (17):

$$\mathcal{L}_{r,i} = \sum_{\mathbf{r}} \left| O_{\mathbf{r}_i}P_{\mathbf{r}} - \psi_{\mathbf{r}_i}^e + O_{\mathbf{r}_i}\alpha_{x,i} \frac{\partial P_{\mathbf{r}}}{\partial x} + O_{\mathbf{r}_i}\alpha_{y,i} \frac{\partial P_{\mathbf{r}}}{\partial y} \right|^2 = \sum_{\mathbf{r}} |\chi_{\mathbf{r}_i}|^2. \quad (19)$$

The shift $\alpha_{x,i}$ (and similarly $\alpha_{y,i}$) can be obtained by differentiating the cost function in equation (19) with respect to $\alpha_{x,i}$ and setting it to zero:

$$\begin{aligned} \frac{\partial \mathcal{L}_{r,i}}{\partial \alpha_{x,i}} &= \sum_{\mathbf{r}} 2\chi_{\mathbf{r}_i} \left(O_{\mathbf{r}_i} \frac{\partial P_{\mathbf{r}}}{\partial x} \right)^* = 0 \\ \sum_{\mathbf{r}} \left((O_{\mathbf{r}_i}P_{\mathbf{r}} - \psi_{\mathbf{r}_i}^e) \left(O_{\mathbf{r}_i} \frac{\partial P_{\mathbf{r}}}{\partial x} \right)^* + \alpha_{x,i} \left| O_{\mathbf{r}_i} \frac{\partial P_{\mathbf{r}}}{\partial x} \right|^2 + \alpha_{y,i} \left| O_{\mathbf{r}_i} \right|^2 \frac{\partial P_{\mathbf{r}}}{\partial x} \frac{\partial P_{\mathbf{r}}}{\partial y} \right) &= 0 \end{aligned} \quad (20)$$

As the gradients along x and y directions are orthogonal, the last term in equation (20) is zero and the translation $\alpha_{x,i}$ is obtained from:

$$\alpha_{x,i} = - \frac{\sum_{\mathbf{r}} \mathcal{R} \left[(O_{\mathbf{r}_i}P_{\mathbf{r}} - \psi_{\mathbf{r}_i}^e) \left(O_{\mathbf{r}_i} \frac{\partial P_{\mathbf{r}}}{\partial x} \right)^* \right]}{\sum_{\mathbf{r}} \left| O_{\mathbf{r}_i} \frac{\partial P_{\mathbf{r}}}{\partial x} \right|^2}. \quad (21)$$

The scanning position vector is updated via $\mathbf{r}_i = \mathbf{r}_i - (\alpha_{x,i}, \alpha_{y,i})$ at every iteration.

Ptychographic position refinement methods have been shown to achieve subpixel accuracy as good as 0.01 pixels^{17,63}. As the reconstructed pixel size depends on the recorded diffraction pattern area, the position refinement step can be performed using cropped diffraction patterns to produce reconstructions with larger pixel size. In doing so, the computational load is decreased as the processed diffraction patterns are smaller. Moreover, diffraction patterns generally have fewer photons at regions corresponding to higher resolution, which are removed during data cropping. Hence, large-pixel-size reconstructions

are not only faster but also more robust while still maintaining sufficient position accuracy.

Phase-residue minimization with refractive index ptychography

When imaging specimens containing small high-contrast features, such as integrated circuits, ptychography can contain phase artefacts within the reconstructed projections. Such artefacts, called phase residues, tend to originate at locations of steep phase gradients commonly found near single-pixel-sized features, for example, at the transistor level. As a result, phase residuals negatively influence the alignment of projections^{24,64}, limit the maximum attainable resolution and introduce visible artifacts. To improve reconstruction quality and minimize the phase residue, we used refractive index ptychography⁶⁵, which directly reconstructs the refractive index of the object such that phase unwrapping is no longer necessary.

Assuming that the sample is optically thin, the reconstructed object provides direct information of the sample's refractive index $n_r = 1 - \delta_r + i\beta_r$ via⁶⁵:

$$O_r = A_r \exp(i\phi_r) = \exp\left(ik \int (n_r - 1) dz\right) = \exp(i\tilde{O}_r). \quad (22)$$

The desired refractive object \tilde{O}_r is a complex quantity whose real and imaginary parts are linked to the X-ray absorption A_r and phase shift ϕ_r via⁶⁵:

$$\mathcal{R}(\tilde{O}_r) = \phi_r = -k \int \delta_r dz, \quad (23)$$

$$\mathcal{I}(\tilde{O}_r) = -\ln(A_r) = k \int \beta_r dz, \quad (24)$$

\mathcal{R} and \mathcal{I} represent the real and imaginary parts, respectively. Typically, obtaining the refractive object \tilde{O}_r requires phase unwrapping algorithms⁶⁵, as the reconstructed phase ϕ_r is an argument of the complex exponential and will be wrapped to a range of 2π . The unwrapping problem can be ill-posed in the presence of phase residuals, where a unique solution no longer exists. One way to mitigate the presence of phase residues within a projection is to reconstruct the refractive object directly using gradient descent⁶⁵:

$$\tilde{O}'_r = \tilde{O}_r - \alpha_i \frac{\partial \mathcal{L}_{r,i}}{\partial \tilde{O}_r}. \quad (25)$$

which is similar to non-refractive index object reconstruction from equation (8). The refractive object cost-function gradient can be calculated as follows:

$$\frac{\partial \mathcal{L}_{r,i}}{\partial \tilde{O}_r} = \frac{\partial \mathcal{L}_{r,i}}{\partial O_r^*} \frac{\partial O_r^*}{\partial \tilde{O}_r} = \frac{\partial \mathcal{L}_{r,i}}{\partial O_r^*} \cdot (iO_r)^*. \quad (26)$$

This shows that the search direction for refractive index ptychography can be computed using previously derived gradients from non-refractive ptychography in equation (12) multiplied by $(iO_r)^*$. Hence, the refractive index object \tilde{O}_r can be updated using existing ptychographic reconstruction algorithms based on the modification shown in equation (26). Once \tilde{O}_r is updated at a given iteration, the remaining computations of a given ptychographic reconstruction algorithm can be carried out using the non-refractive object function $O_r = \exp(i\tilde{O}_r)$.

Burst ptychography

Burst ptychography is a new image acquisition and reconstruction variant of ptychography, where for each position in a point-by-point scan, multiple low-exposure frames are captured, each with exposure times on the order of a few milliseconds. Compared with conventional

ptychography, the total exposure time is preserved to accumulate the necessary photon dose. This allows resolving the temporal dynamics of experimental instabilities and decoupling of them across multiple exposures, which would otherwise blur the diffraction patterns, as shown in Fig. 1c. An alternative method is mixed-state ptychography³³, which can account for various experimental inconsistencies, such as X-ray beam instabilities, using multiple mutually incoherent probe modes during ptychographic reconstruction. However, the need to identify and correct instabilities superimposed onto a single detector frame leads to lower reconstruction resolution and overall quality owing to reduced speckle contrast³⁶. However, in burst ptychography, the recording of time-resolved diffraction patterns significantly increases the amount of raw data, computational processing and memory requirements. In addition, the poorer signal-to-noise ratio (SNR) of each low-exposure image reduces computational convergence.

We circumvent these issues in two ways. First, we identify and group similar frames after recovering the true scanning positions using the computational refinement algorithm described in the 'Position refinement algorithm' section. Once the groups are found, they can be summed to increase the SNR of each individual frame and also reduce the overall computational requirements for phase retrieval. For each collected image, the ptychographic reconstruction executes computationally expensive Fourier transforms and imposes real and reciprocal-space constraints. By summing the matching burst frames, the computational burden is reduced owing to the use of fewer images in the reconstruction. Second, we use an incremental, or pyramidal, reconstruction workflow where low-complexity and low-resolution reconstructions are completed first, followed by gradual refinement with more algorithmic degrees of freedom. This is especially important for noisy data when applying a mixture of competing algorithms, such as orthogonal probe relaxation³⁴, mixed states³³ and position refinement¹⁷, in parallel rather than sequentially. Hence, even in the case of non-repeatable instabilities where frame identification and summation is less effective, the presented reconstruction and data acquisition approaches are still valid.

To mitigate the effects of instabilities, boost algorithm convergence and reduce computational load, we introduce a specialized four-step reconstruction process, outlined in Extended Data Fig. 3:

1. Initialize the reconstruction. First, we find a good initial estimate of the object by summing all burst frames for each scan position and performing a conventional ptychographic reconstruction. Because of the measurement instabilities, the summed diffraction patterns become blurred, which leads to lower reconstruction quality. However, the significantly reduced data quantity allows a quick reconstruction of the object estimate that is used as a starting point for the remainder of the reconstruction.
2. Find the scanning instabilities within each scan position. Second, to perform the position search, we use cropped diffraction data, illustrated by Extended Data Fig. 3a. Although data cropping reduces the maximum attainable resolution, it offers a robust, fast and memory-efficient way to perform position refinement (Extended Data Fig. 3b). As the position refinement method achieves subpixel accuracy (as described in the 'Position refinement algorithm' section), data cropping is done without adverse effects to the reconstruction quality. If all the scan points suffer from the same repeatable instabilities, then an optional regularization step can be applied to improve convergence. This is achieved by gathering all burst position groups from each of the scans and imposing a low-rank approximation using singular value decomposition⁶⁶ at each iteration of position refinement.
3. Identify and sum matching burst frames. Third, we perform burst-frame matching based on the similarity of the refined positions. If the distance between the refined positions is less than or equal to a pixel (4.2 nm), the corresponding frames are considered similar and summed, as shown in Extended Data Fig. 3c. In doing so, the SNR of the 'matching' diffraction data is increased, and the computational burden

Article

is minimized owing to reduced data quantities. Despite the lower SNR, the unmatched frames are still included in the reconstruction. Because resolution improves with added radiation dose¹¹, these frames also positively contribute to the photon statistics of the measurement and improve the resolution. SNR variations between the processed images will affect the convergence of ptychographic reconstruction, which can be enhanced by the implementation of an adaptive step-size strategy. This strategy fine-tunes the steps during each iteration, tailoring them to the underlying SNR of each respective image. To achieve this, we use an iterative least-squares maximum-likelihood solver¹⁷, which computes the optimal step size for each image. This approach is similar to the adaptive step-size techniques found in Fourier ptychographic microscopy⁶⁷, designed to mitigate the substantial differences in photon counts between collected bright-field and dark-field images.

4. Reconstruct the data using refined position and grouped burst frames. The fourth and final high-resolution phasing step is performed to refine the prior lower-resolution reconstructions from step 1 using the full-size diffraction patterns. The refined positions are used from step 2 together with the summed frames from step 3 to obtain reconstruction with the highest possible resolution.

Ptychographic data reconstruction

To reconstruct the data with a 4.2-nm pixel size, 500×500 pixels of the total detector array were processed using the PtychoShelves reconstruction package⁶². All reconstruction steps used the difference map¹⁶ and LSQML engines¹⁷, found in the PtychoShelves reconstruction software⁶². Two probe modes³³ were used to account for inconsistencies between the collected data and the idealized forward model, such as parasitic scattering⁶⁸ and partial spatial coherence³³. Rather than starting with a flat object initialization, the object was initialized by estimating the amplitude and phase from the collected diffraction patterns⁶⁹.

For the burst reconstruction method, a conventional ptychographic reconstruction was performed after the summation of the burst frames, with 300 iterations using the difference map and 300 iterations using LSQML engines. Next, to identify the matching burst frames, the 23 burst images for each scanning point (around 8,000 diffraction patterns per projection) were considered. To fit all of these images on a single graphics processing unit (NVIDIA A100) for fast data processing, burst-frame identification was performed on a reduced detector area consisting of 200×200 pixels. To identify similar burst frames, 50 iterations of ptychographic position optimization were performed¹⁷. Following burst-frame identification and matching, the data size was reduced to about 60%, for which we used 150 iterations of LSQML to refine the ptychography reconstructions. On a single NVIDIA A100 graphics processing unit card, the total reconstruction time took around 800 s per projection. To mimic and compare with conventional ptychographic reconstructions, the 23 burst frames were summed to produce long-exposure images affected by motion-induced blurring. The reconstructions were performed equivalently to burst ptychography, except using 1,000 iterations instead of 150 for the last LSQML refinement step. These reconstructions were performed with two and six probe modes³³ to take into account possible experimental inconsistencies such as limited illumination coherence and experimental instabilities. Reconstructions with six-probe mixed-state modes showed better results and were used for comparison with burst ptychography in the ‘Comparison between burst and mixed-state ptychography’ section.

Tomographic reconstruction

In this paper, we imaged a sample with 5-μm diameter, which is an order of magnitude larger than the bound T for sample thickness imposed by the image depth of field, given by⁵²:

$$T \leq 5.2r^2/\lambda, \quad (27)$$

where λ is the X-ray wavelength and r is the resolution. Given X-rays with 6.2-keV photon energy and a resolution of 4.2 nm, $T \leq 0.5 \mu\text{m}$. Exceeding the depth of field affects the resolution across the sample and in some cases can complicate ptychographic and tomographic reconstructions.

For thicker samples, where multiple scattering is likely, multi-slice ptychography is typically required^{52,53}. This technique can account for the wavefront scattering multiple times within the sample. Here we opted for single-slice ptychography, assuming minimal multiple scattering, and addressed depth-of-field issues during tomographic reconstruction with a filtered back-propagation algorithm, which is commonly used in optical diffraction tomography^{4,21}. This method is suitable for weak-to-moderate scattering samples and can be accurately implemented using angular-spectrum or Fresnel propagators. The back-propagation through the sample ensures that wavefront changes during propagation are incorporated into the tomographic reconstruction. Hence, our approach differs from the standard back-projection tomography where the projections are simply projected through the sample volume, neglecting propagation effects. The separation of the illumination wavefront from the complex-valued projections during ptychographic reconstruction eliminates the need for Rytov or Born corrections used in optical diffraction tomography^{4,21}.

Our filtered back-propagation reconstruction algorithm for 3D data follows the general approach of optical diffraction tomography⁴:

1. Digitally refocus the complex-valued projection to the sample centre.
2. Propagate the projection through the sample from $-t/2$ to $t/2$ (t is sample thickness).
3. Extract phase or absorption images, with phase unwrapping for phase tomography.
4. Filter the images as in filtered back-projection.
5. Rotate and add the filtered, back-propagated stack into the tomogram.

This process differs from the conventional filtered back-projection algorithm, where the initial steps of refocusing and propagation are not necessary. Refocusing is crucial because the plane of the reconstruction is not necessarily at the middle of the sample, owing to the sample significantly exceeding the depth of field. We determined the optimal propagation distance for every reconstructed projection by finding the propagation distance with the maximum image sharpness, a metric and method similar to those used by auto-focusing in digital cameras. Sharpness estimation involved propagating projections through the sample volume and using the standard deviation of a high-pass filtered image as a sharpness metric. This method outperformed other metrics such as total variation, which has been suggested for ptychography⁷⁰. The sharpness versus propagation distance was fitted to a Gaussian curve to precisely determine the optimal focus distance and reduce the influence of outliers^{71,72}. After identifying optimal propagation distances, each projection was propagated to the sample centre using the angular-spectrum method. The subsequent reconstruction steps follow the filtered back-projection tomography outlined above.

The results of digital refocusing algorithms can in principle be skewed by the Talbot effect⁷³, where at certain distances the pitch of periodic structures will become smaller and such images will appear sharper. Given an image pixel size of 4.2 nm, the smallest resolvable period due to the fractional Talbot effect will be 8.4 nm, which will occur at propagation distances $z = 16.8 \text{ nm} \times a/\lambda$, where a is the period of a structure and λ is the wavelength of the X-rays⁷³. In our sample, fins are structures with the smallest period of 30 nm, which yields the smallest fractional Talbot distance of 2.5 μm. As our refocusing algorithm estimated optimal refocusing values to be around 1–2 μm, the Talbot effect did not affect the optimal propagation estimation. It is noted that the smallest fractional Talbot distances will increase for other structures of the integrated circuits, such as the gates with a period of 60 nm, making the effect prominent for only small features such as the fins. Given the relatively minuscule area of the fins with respect

to the whole sample, even in the presence of Talbot effects the digital refocusing would be unaffected in our case.

For this study, 1,700 ptychographic projections were collected as a series of tomograms with sequential angular offsets⁷⁴. The reconstructed projections were aligned using vertical mass fluctuation and tomographic consistency methods^{24,64} before the filtered back-propagation tomographic reconstruction. To our knowledge, this is the first use of filtered back-propagation algorithm for PXCT and it was able to greatly improve the depth of field of the reconstructed tomogram as illustrated by Extended Data Fig. 4.

Comparison between burst and mixed-state ptychography

To compare the performance of burst and mixed-state ptychography, all PXCT projections were reconstructed by summing the burst frames to mimic a conventional ptychography acquisition. Better results were obtained for mixed-state reconstruction using six-probe modes, instead of two used for burst ptychography, and 6.5-times higher iteration number to increase the likelihood of recovering the vibrational modes. The use of mixed-state ptychography modes is motivated by the observations from fly-scan ptychography, where mixed-state ptychography is able to mitigate diffraction pattern blurring caused by intentionally translating the sample during data acquisition^{29,30,75}. As shown in Extended Data Fig. 5a,b, burst ptychography has superior image quality, compared with mixed-state ptychography, based on the resolution of the gates and the source and drain contacts with a characteristic 59-nm pitch. Beam instabilities are also reflected by the probe modes shown in Extended Data Fig. 5d,e for one projection, where for burst ptychography the main mode power is 93% whereas for mixed-state ptychography it is only 43%, while the remaining modes have a power of 29%, 10%, 8%, 6% and 4%. Moreover, the second probe mode is elongated along the diagonal direction, which matches the direction of the beam instabilities shown in Extended Data Fig. 5c. As the illumination coherence fraction is the same within both reconstructions, the higher power of the additional probe modes is associated with inconsistencies between the experimental data and the forward model, such as illumination instabilities. Compared with the reduced quality of mixed-state reconstruction in Extended Data Fig. 5a,b, burst ptychography provides a successful method for instability correction.

Elemental composition of the integrated circuit

EDX was performed on the thin lamella from the integrated circuit sample prepared for transmission electron microscopy to identify the elemental composition. The elemental map of the integrated circuit is shown in Extended Data Fig. 6a, highlighting the presence of Cu interconnects and dielectric elements (O and Si). While the relative quantities of Si surrounding the global and non-global interconnects remain constant, the amount of O is greatest at the global interconnect layer. Such differences indicate the presence of two different dielectric materials supporting the segmented volumes by PXCT in Fig. 5a,b. Under increased magnification, the non-global interconnects (metal layers M0–M10) in Extended Data Fig. 6b show that the Cu appears to be doped with elements such as Co, Fe and Al. Moreover, these elements are known to minimize void formation caused by charge migration⁴⁵. At the front-end-of-line transistor layer shown in Extended Data Fig. 7, the source and drain contacts use Co instead of Cu while the gates contain Ti, Al and traces of Cu. In Extended Data Figs. 6 and 7, the high-contrast, high-resolution overview images were acquired using HAADF-STEM rather than BF-STEM used for Fig. 3. This decision was motivated by the fact that the image contrast in HAADF-STEM is sensitive to the square of the atomic number⁷⁶, which aids in highlighting elemental differences.

Resolution estimation

FSC⁷⁷ analysis is a standard resolution estimation for two-dimensional or 3D datasets. This method calculates correlations in the Fourier domain by taking rings (for two-dimensional data) or shells (for 3D

data) of progressively increasing spatial frequencies from two independent datasets. In doing so, correlation at every spatial frequency region is calculated to produce a plot such as in Extended Data Fig. 8a. A one-dimensional plot from two-dimensional or 3D datasets is obtained by averaging the rings or shells to estimate the average resolution of a pixel or voxel. Once the FSC value drops below a selected threshold⁷⁷, it indicates that spatial frequencies beyond this cut-off represent noise and sets an estimate of the maximum resolvable features within the data. To estimate the resolution of our tomogram, the reconstructed 1,700 projections were divided in half to produce two independent tomograms spanning the full 180° angular range. An alternative approach would be to acquire two independent tomograms of the same sample, but given the long image acquisition times of tomographic experiments and effects of radiation damage, the practical approach is to split the collected data in half without the loss of estimation accuracy. This approach then gives an upper, that is, pessimistic, bound to the resolution estimation.

Extended Data Fig. 8 shows FSC analysis of the two tomograms, demonstrating that the estimated half-period resolution is 4.2 nm, limited by the reconstructed pixel size. These results were complemented by resolution estimates based on 25–75% edge profile analysis⁴² from the reconstructed tomogram shown in Extended Data Fig. 8c. Edge sharpness, however, depends not only on the resolution of the imaging system but also on the relative contrast between the features used for analysis. Hence, while edge profiles give an average resolution estimate of around 4.7 nm, these measurements are conservative, supporting the FSC analysis.

Data availability

Recorded diffraction patterns, reconstructed ptychographic projections, reconstructed tomograms and accompanying codes are available at <https://doi.org/10.16907/33321c7a-f6bf-441e-8ae4-3f4cabd2dc0d>.

Code availability

Standalone codes are available at <https://doi.org/10.16907/4c56cb87-d73f-402d-96c9-d5e6736fc8a3>.

55. Holler, M. et al. Environmental control for X-ray nanotomography. *J. Synchrotron Radiat.* **29**, 1223–1231 (2022).
56. Guizar-Sicairos, M. et al. Role of the illumination spatial-frequency spectrum for ptychography. *Phys. Rev. B* **86**, 100103 (2012).
57. Dinapoli, R. et al. EIGER: next generation single photon counting detector for X-ray applications. *Nucl. Instrum. Methods Phys. Res. A* **650**, 79–83 (2011).
58. Huang, X. et al. Optimization of overlap uniformness for ptychography. *Opt. Express* **22**, 12634–12644 (2014).
59. Yeh, L.-H. et al. Experimental robustness of Fourier ptychography phase retrieval algorithms. *Opt. Express* **23**, 33214–33240 (2015).
60. Loetgering, L. et al. PtyLab.m/py/l: a cross-platform, open-source inverse modeling toolbox for conventional and Fourier ptychography. *Opt. Express* **31**, 13763–13797 (2023).
61. Fienup, J. R. Phase retrieval algorithms: a comparison. *Appl. Opt.* **21**, 2758–2769 (1982).
62. Wakonig, K. et al. PtychoShelves, a versatile high-level framework for high-performance analysis of ptychographic data. *J. Appl. Crystallogr.* **53**, 574–586 (2020).
63. Zhang, F. et al. Translation position determination in ptychographic coherent diffraction imaging. *Opt. Express* **21**, 13592–13606 (2013).
64. Guizar-Sicairos, M. et al. Phase tomography from X-ray coherent diffractive imaging projections. *Opt. Express* **19**, 21345–21357 (2011).
65. Wittwer, F. et al. Phase retrieval framework for direct reconstruction of the projected refractive index applied to ptychography and holography. *Optica* **9**, 295–302 (2022).
66. Brunton, S. L. & Kutz, J. N. *Data-Driven Science and Engineering: Machine Learning, Dynamical Systems, and Control* (Cambridge Univ. Press, 2019).
67. Zuo, C., Sun, J. & Chen, Q. Adaptive step-size strategy for noise-robust Fourier ptychographic microscopy. *Opt. Express* **24**, 4960–4972 (2016).
68. Enders, B. et al. Ptychography with broad-bandwidth radiation. *Appl. Phys. Lett.* **104**, 171104 (2014).
69. Wittwer, F. et al. Ptychographic reconstruction with object initialization. *Opt. Express* **30**, 33652–33663 (2022).
70. Loetgering, L., Du, M., Eikema, K. S. E. & Witte, S. zPIE: an autofocusing algorithm for ptychography. *Opt. Lett.* **45**, 2030–2033 (2020).
71. Pertuz, S., Puig, D. & Garcia, M. A. Analysis of focus measure operators for shape-from-focus. *Pattern Recognit.* **46**, 1415–1432 (2013).
72. Pertuz, S., Puig, D. & Garcia, M. A. Reliability measure for shape-from-focus. *Image Vis. Comput.* **31**, 725–734 (2013).

Article

73. Berry, M. V. & Klein, S. Integer, fractional and fractal Talbot effects. *J. Mod. Opt.* **43**, 2139–2164 (1996).
74. Kaestner, A. P., Munch, B. & Trtik, P. Spatiotemporal computed tomography of dynamic processes. *Opt. Eng.* **50**, 123201 (2011).
75. Deng, J. et al. Continuous motion scan ptychography: characterization for increased speed in coherent X-ray imaging. *Opt. Express* **23**, 5438–5451 (2015).
76. Kübel, C. et al. Recent advances in electron tomography: TEM and HAADF-STEM tomography for materials science and semiconductor applications. *Microsc. Microanal.* **11**, 378–400 (2005).
77. van Heel, M. & Schatz, M. Fourier shell correlation threshold criteria. *J. Struct. Biol.* **151**, 250–262 (2005).

Acknowledgements Tomography experiments were performed at the coherent small-angle X-ray scattering (cSAXS) beamline, located at the Swiss Light Source of the Paul Scherrer Institut in Villigen PSI, Switzerland. We thank S. Stutz for his support with sample preparation; and C. Appel and J. Ihli for discussions regarding quantitative data interpretation. The STEM/EDX analysis and preparation of the pillar-specimen and lamella for electron microscopy was carried out at the Electron Microscopy Facility at PSI. We thank A. Kubec and XRnanotech for support and manufacturing of the aberrated Fresnel zone plates. The work of T.A. is supported by funding from the Swiss National Science Foundation (SNF), project number 200021_196898. N.W.P. has received funding from the European Union's Horizon 2020 research and innovation programme under the Marie Skłodowska-Curie grant agreement

number 884104. G.A. is supported by the European Research Council under the European Union's Horizon 2020 research and innovation programme, within the Hidden, Entangled and Resonating Order (HERO) project with grant agreement 810451. The transmission electron microscopy/STEM was co-funded by SNF R'Equip Project 206021_177020.

Author contributions M.H., A.D., M.G.-S., G.A., T.A. and A.F.J.L. conceptualized the project. M.H., N.W.P., M.G.-S. and T.A. carried out the PXCT experiments. T.A., M.H., M.G.-S., N.W.P., G.A. and A.D. interpreted the results. E.M. and E.P. prepared the electron microscopy samples. E.P. collected and analysed the high-resolution STEM and EDX data. T.A. and M.G.-S. developed the computational reconstruction methods and T.A. implemented them into PtychoShelves. T.A. reconstructed the projections and tomograms. T.A. made the figures and videos. All authors contributed to the writing of the paper.

Competing interests The authors declare no competing interests.

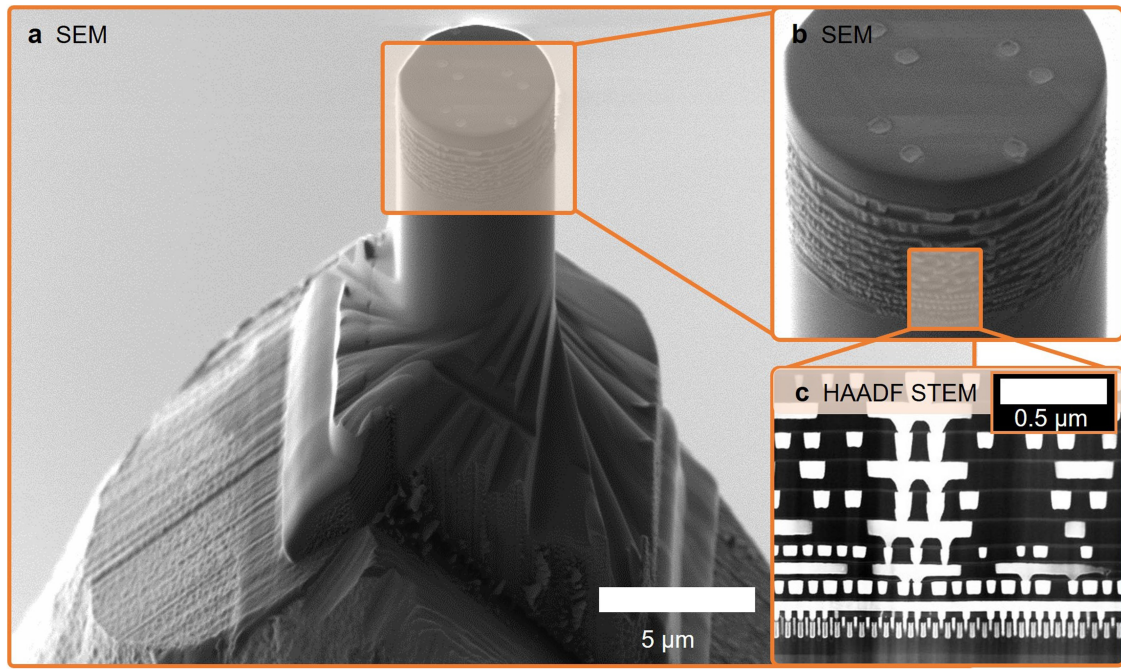
Additional information

Supplementary information The online version contains supplementary material available at <https://doi.org/10.1038/s41586-024-07615-6>.

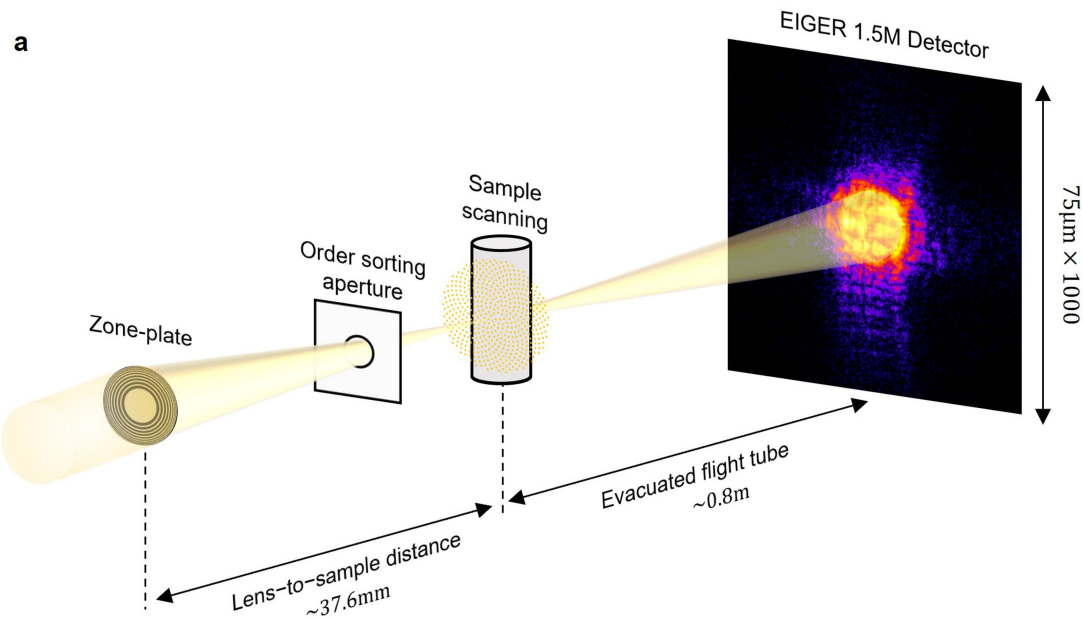
Correspondence and requests for materials should be addressed to Tomas Aidukas or Mirko Holler.

Peer review information *Nature* thanks Chao Zuo and the other, anonymous, reviewer(s) for their contribution to the peer review of this work.

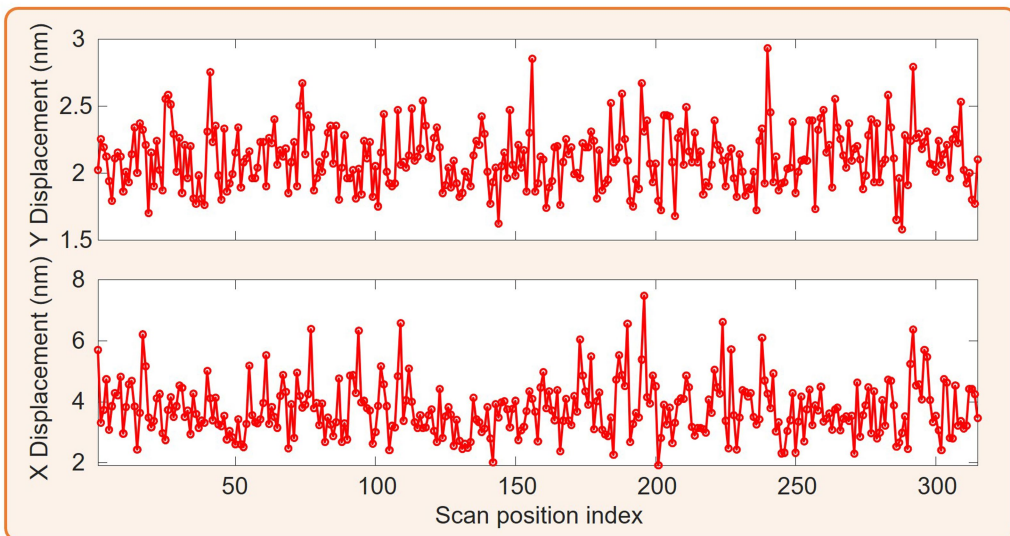
Reprints and permissions information is available at <http://www.nature.com/reprints>.



Extended Data Fig. 1 | Electron microscopy images of the integrated circuit sample. **a,b**, Image of the sample prepared using FIB-SEM. The high-resolution image in **c** was obtained using HAADF STEM. The HAADF STEM image is from a different sample than the one shown in **a,b**.

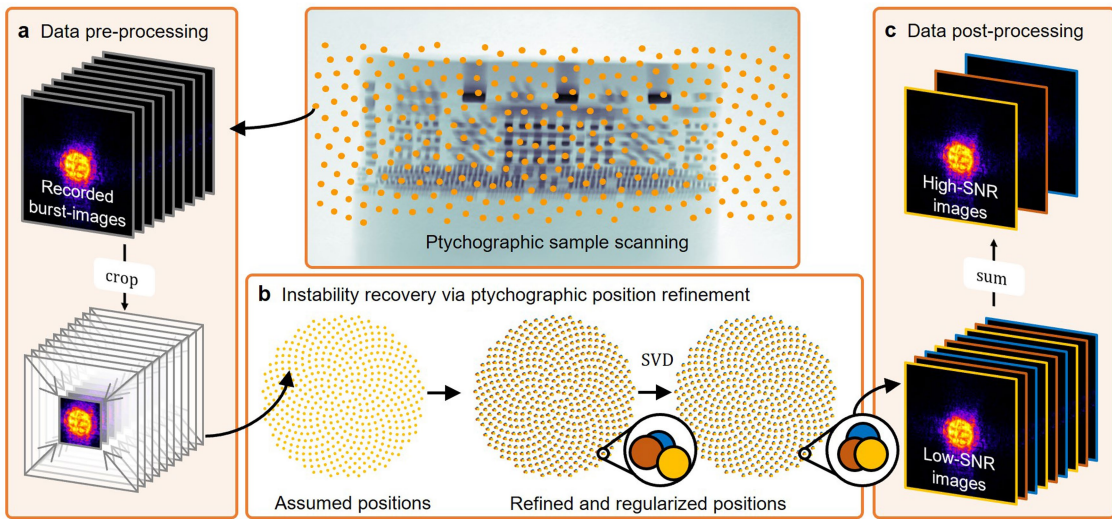


b Sample scanning interferometric stability



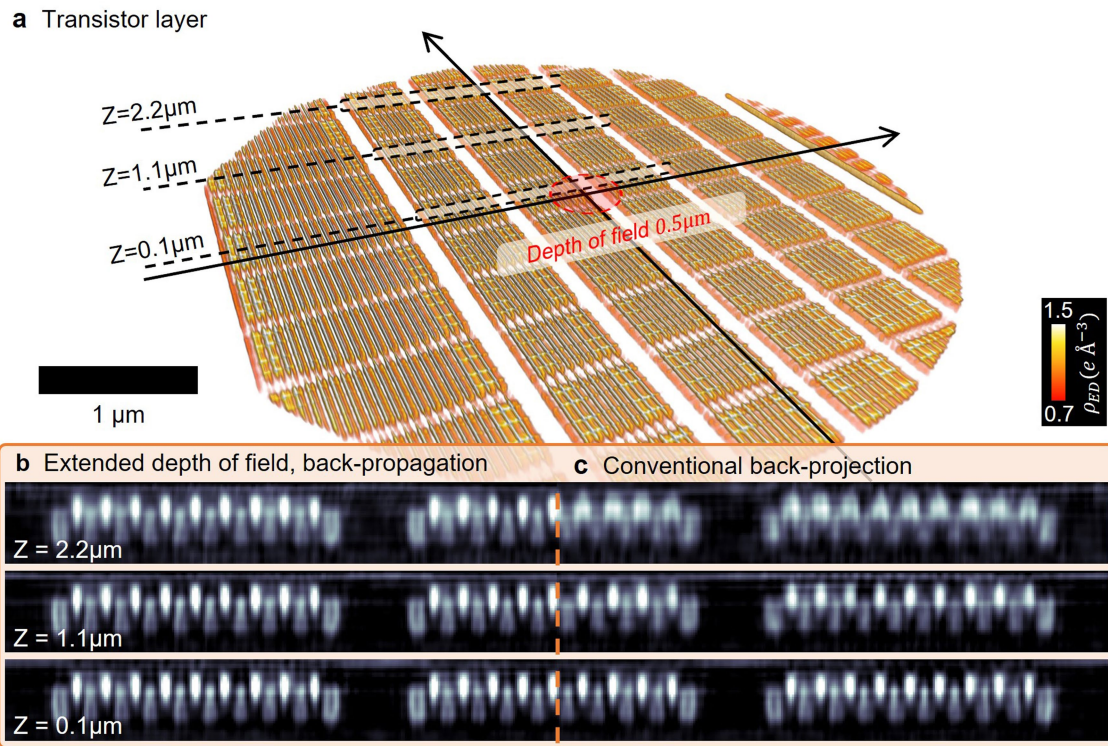
Extended Data Fig. 2 | Experimental setup geometry and sample scanning stability. **a**, Experimental setup geometry used for the ptychographic imaging. The $0.7\text{ }\mu\text{m}$ diameter X-ray beam was created by placing the sample 0.1 mm away from focus (focal length of the Fresnel zone plate is 37.5 mm). Light scattered by the sample propagates through a 0.8 m long evacuated flight tube towards an

in-vacuum EIGER detector. **b**, Average sample scanning stability at every scan position measured by an interferometer operating at 3.5 kHz . The instabilities are plotted as standard deviations from the mean nominal position. During the acquisition of a single projection, the average instability was only up to 4 nm , below the imaging resolution of 4.2 nm .



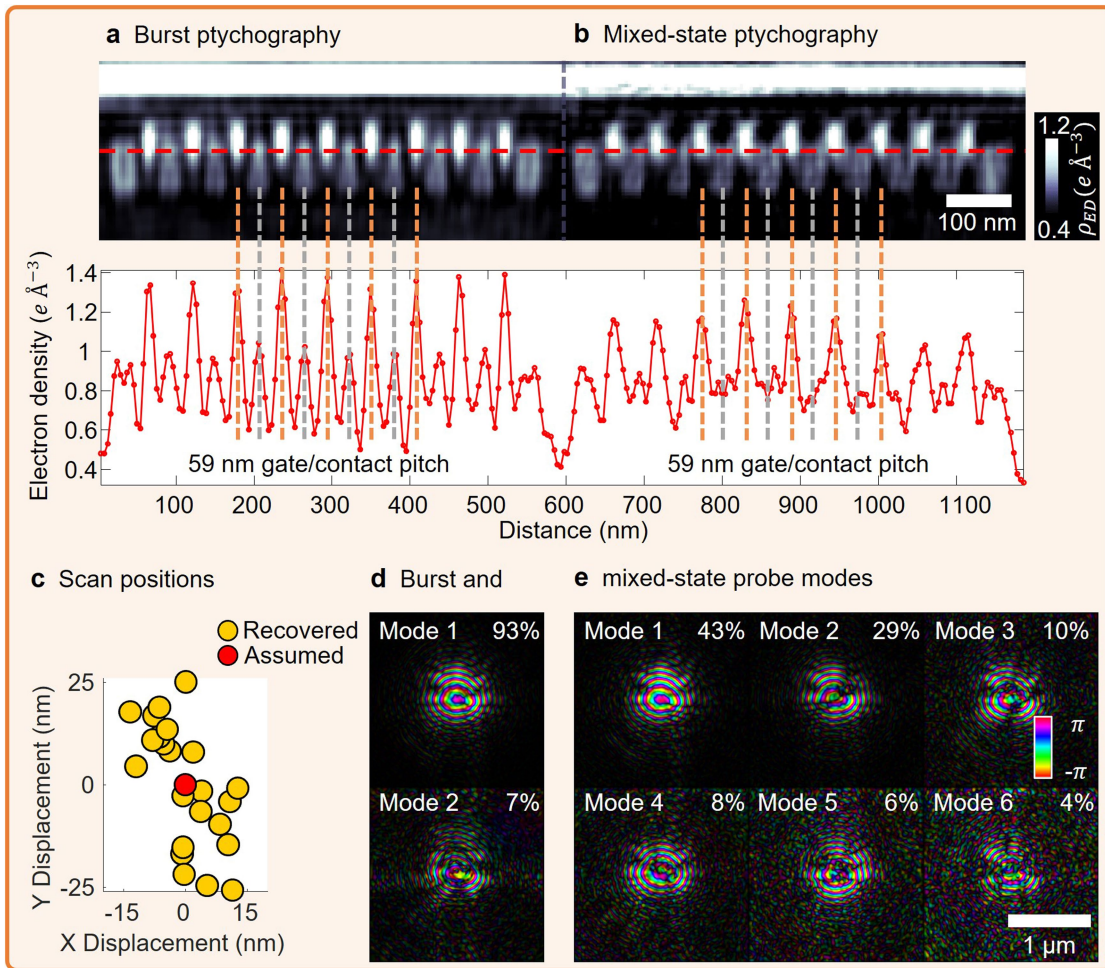
Extended Data Fig. 3 | Burst ptychography data reconstruction pipeline. **a**, For computationally efficient burst frame processing, the recorded burst frame area is cropped. **b**, Next, position refinement is performed on all burst frames to recover the refined positions of the object relative to the probe for each burst frame. In the presence of semi-repeatable instabilities, a low-rank

constraint using singular value decomposition (SVD) is imposed to aid convergence of problematic scan areas. **c**, Once refined positions are identified, the matching burst-frames are summed to increase the SNR of the frames and decrease the computational burden.



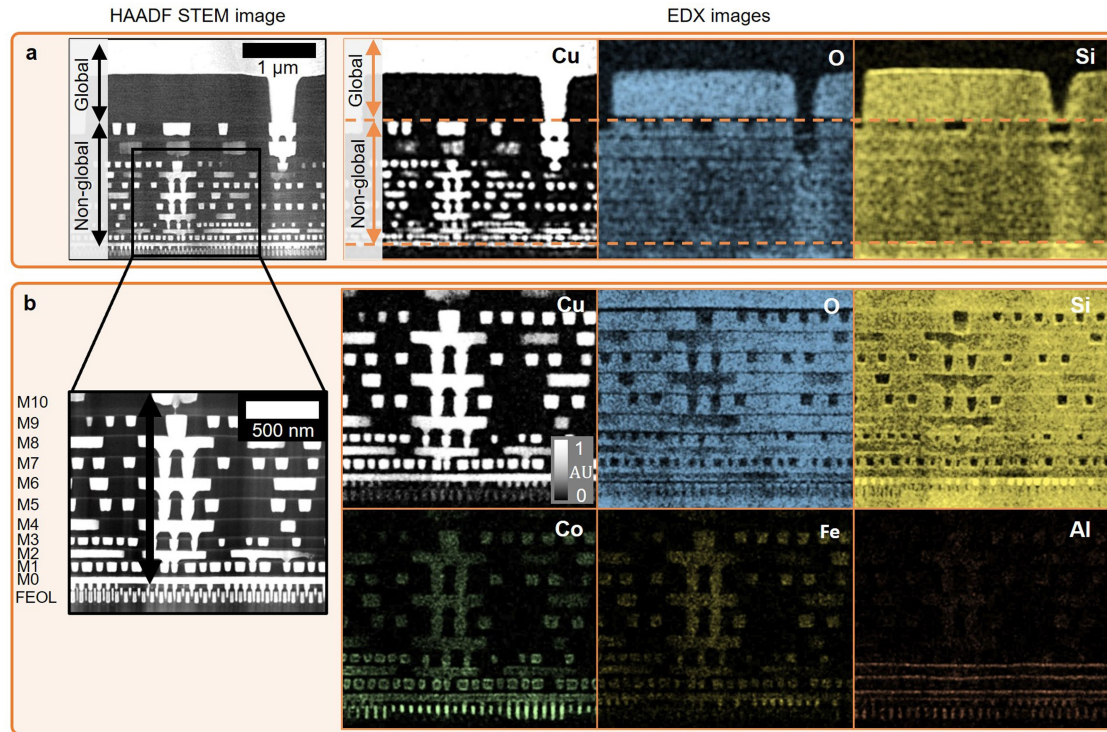
Extended Data Fig. 4 | Extended depth-of-field tomography using filtered back-propagation. **a**, Rendering of the tomogram's transistor layer, which was reconstructed using the filtered back-propagation tomography algorithm to extend the depth-of-field. This method ensures uniform image quality across

the entire volume, as illustrated in **b**, whereas with conventional back-projection reconstruction image quality notably diminishes beyond a depth of field of 0.5 μm, as demonstrated in **c**.



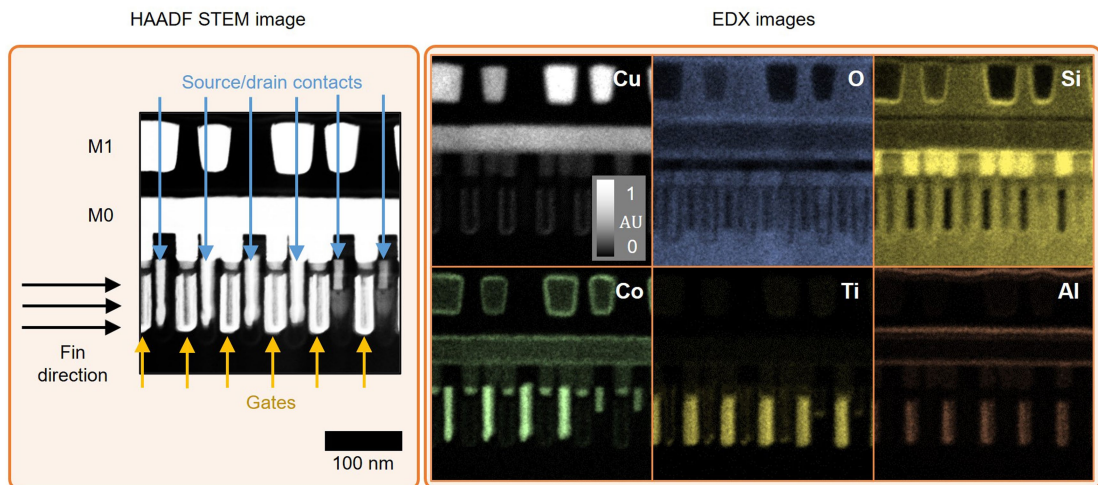
Extended Data Fig. 5 | Reconstruction quality evaluation between burst and non-burst ptychography. Comparison between burst ptychography in **a** and mixed-state ptychography in **b** shows that the gates and contacts at the transistor layer are well resolved with burst ptychography, which is not the case when using mixed-state ptychography. This discrepancy indicates that the

additional probe modes in mixed-state ptychography are trying to account for the unknown instabilities, which were recovered with burst ptychography and are shown for a single scan position in **c** (taken from Fig. 2). Additionally, the main probe mode power of burst ptychography in **d** is 93%, whereas for mixed-state ptychography in **e** it is only 43%.



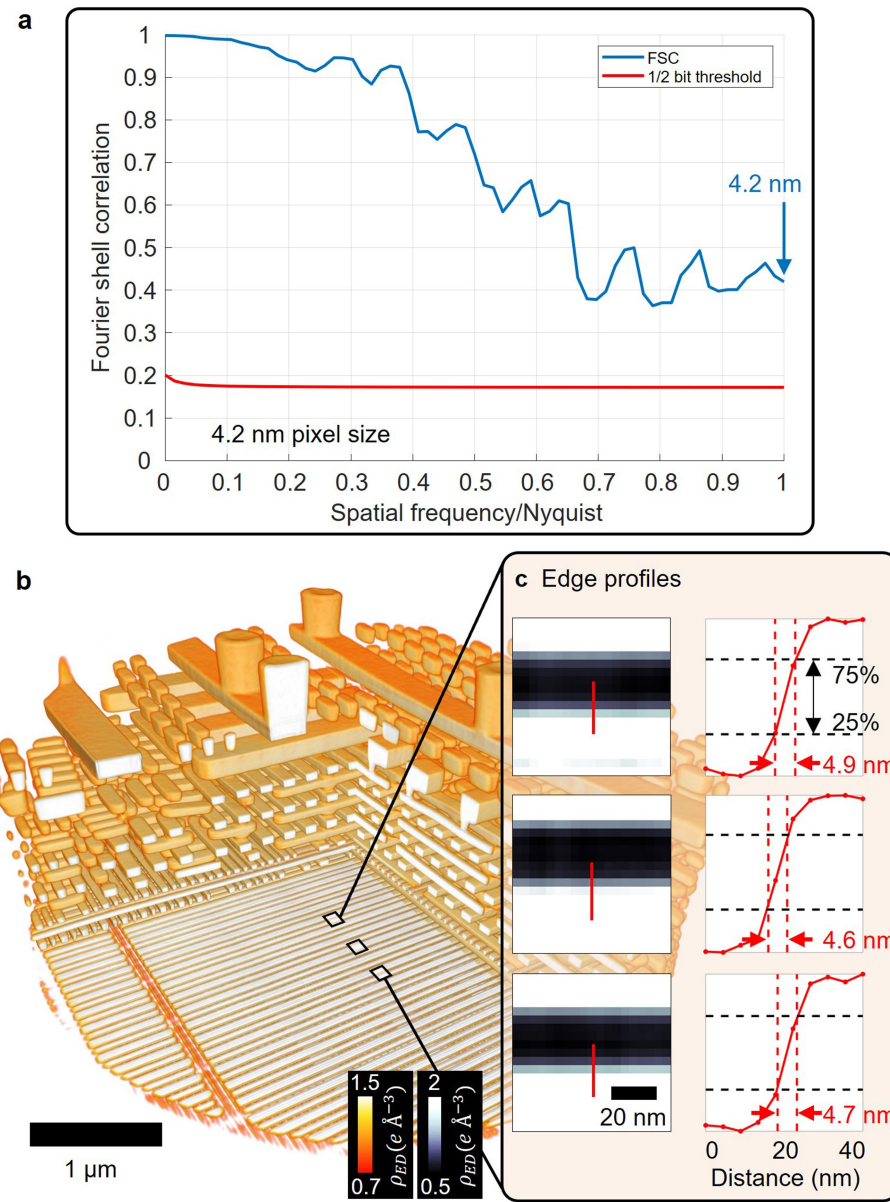
Extended Data Fig. 6 | Integrated circuit elemental composition analysis using EDX. **a**, Throughout the IC, the most abundant elements are Cu (for the interconnects) and Si, O for the surrounding dielectric. The concentration of O is higher at the global interconnect layer compared to the other layers, indicating the presence of two dielectric materials which are separated by

dashed lines. **b**, Increased magnification within the non-global layers shows material differences between the interconnect and transistor layers. The element concentration is plotted on a relative scale, in arbitrary units, with respect to each other.



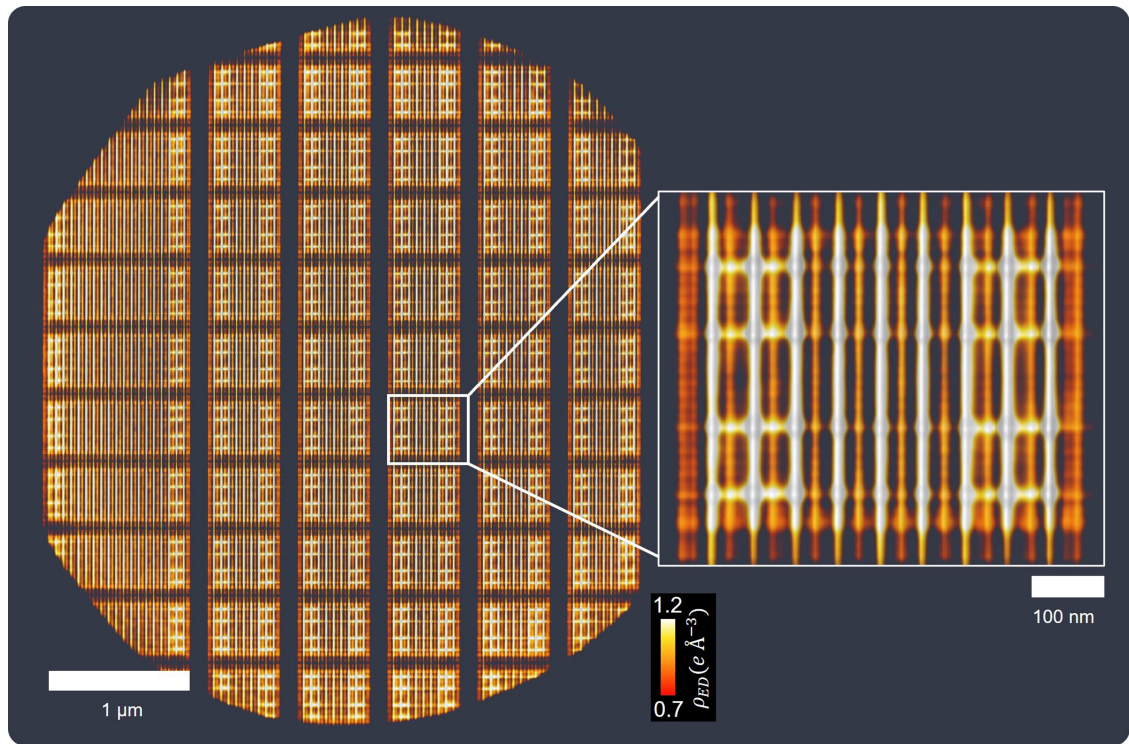
Extended Data Fig. 7 | Transistor elemental composition analysis using EDX. EDX analysis of the transistor layer perpendicular to the fin direction. Source/drain contacts contain mostly Co, while the gates consist of Ti and Al.

There is a significant concentration of Si between the interconnects and contacts/gates. The element concentration is plotted on a relative scale, in arbitrary units, with respect to each other.



Extended Data Fig. 8 | Resolution analysis using FSC and edge profiles.
a, Fourier shell correlation (FSC) of the reconstructed tomogram showing a pixel-limited half-pitch resolution of 4.2 nm. **b**, Copper interconnects were

used for edge profile analysis in **c**, which supports the half-pitch resolution estimation by FSC based on the 25–75 edge criterion.



Extended Data Fig. 9 | Rendering of the sample’s transistor layer. Top view of the transistor layer, where the “unit cell” element is repeated throughout the whole layer. See Supplementary Videos 3–4 for a 3D visualization of the transistor layer and the unit cell.